



Ghani, Irfan, Koehn, Daniel, Toussaint, Renaud, and Passchier, Cees Willem (2013) *Dynamic development of hydrofracture*. Pure and Applied Geophysics, 170 (11). pp. 1685-1703. ISSN 0033-4553

Copyright © 2013 Springer Verlag

A copy can be downloaded for personal non-commercial research or study, without prior permission or charge

Content must not be changed in any way or reproduced in any format or medium without the formal permission of the copyright holder(s)

When referring to this work, full bibliographic details must be given

<http://eprints.gla.ac.uk/83062/>

Deposited on: 31 March 2014

1 **Title:**

2 **Dynamic Development of Hydrofracture**

3

4 **Authors:**

5 Irfan Ghani

6 Tektonophysik, Institut für Geowissenschaften, Johannes Gutenberg Universität Mainz,
7 Germany.

8 Daniel Koehn

9 School of Geographical and Earth Sciences, University of Glasgow, UK.

10 Renaud Toussaint

11 Institute of Globe Physics in Strasbourg, CNRS / University of Strasbourg, 5 rue
12 Descartes, 67084 Strasbourg Cedex, France

13 & Centre for Advanced Study at the Norwegian Academy of Science and Letters,
14 Drammensveien 78, 0271 Oslo, Norway.

15 Cees Willem Passchier

16 Tektonophysik, Institut für Geowissenschaften, Johannes Gutenberg Universität Mainz,
17 Germany.

18

19 **Key Point:**

20 Hybrid discrete-continuum formulation is developed to model natural hydro-driven fracturing.

21 Pore pressure diffusion is crucial in pattern formation.

22

23 **Abstract:**

1 Many natural examples of complex joint and vein networks in layered sedimentary rocks are
2 hydro-fractures that form by a combination of pore fluid overpressure and tectonic stresses. In
3 this paper, a two-dimensional hybrid hydro-mechanical formulation is proposed to model the
4 dynamic development of natural hydrofractures. The numerical scheme combines a Discrete
5 Element Model (DEM) framework that represents a porous solid medium with a supplementary
6 Darcy based pore-pressure diffusion as continuum description for the fluid. This combination
7 yields a porosity controlled coupling between an evolving fracture network and the associated
8 hydraulic field. The model is tested on some basic cases of hydro-driven fracturing commonly
9 found in nature i.e., fracturing due to local fluid overpressure in rocks subjected to hydrostatic
10 and nonhydrostatic tectonic loadings. In our models we find that seepage forces created by
11 hydraulic pressure gradients together with poroelastic feedback upon discrete fracturing play a
12 significant role in subsurface rock deformation. These forces manipulate the growth and
13 geometry of hydrofractures in addition to tectonic stresses and the mechanical properties of the
14 porous rocks. Our results show characteristic failure patterns that reflect different tectonic and
15 lithological conditions and are qualitatively consistent with existing analogue and numerical
16 studies as well as field observations. The applied scheme is numerically efficient, can be applied
17 at various scales and is computational cost effective with the least involvement of sophisticated
18 mathematical computation of hydrodynamic flow between the solid grains.

19

20 **Index Terms:**

21 0500 COMPUTATION GEOPHYSICS

22 0545 Modeling

23 0550 Model verification and validation

- 1 0560 Numerical solutions
- 2 5100 PHYSICAL PROPERTIES OF ROCKS
- 3 5104 Fracture and flow
- 4 5112 Microstructure
- 5 5114 Permeability and porosity

6

7 **Keywords:**

8 DEM, Hydrofracture, fluid-solid dynamics, pore pressure diffusion, pattern formation.

9

10 **1) Introduction:**

11 Brittle deformation of rocks in association with over pressured fluid plays an important
12 role in the geophysical, geochemical and structural mechanics of the Earth's crust in a wide
13 variety of geological settings [Fyfe *et al.*, 1978]. A number of fluid expansion mechanisms e.g.,
14 burial compaction, clay dehydration, organic matter decomposition and aquathermal expansion
15 as well as impermeable rock units which behave as seal to subterranean fluid flow render the
16 pore fluid overpressure, which if in excess of the least principal stress ($P_f > \sigma_3$) may lead to load
17 parallel or load oblique tension fracturing (figure 1) in depths of the Earth's crust.

18

19 **(Figure – 1)**

20

21 The mechanism of hydrofracturing has great implications in the interpretation of field
22 observations and for the prediction of natural or industrial problems in a broad range of research
23 disciplines. After pioneering work of [Hubbert and Willis, 1957; Hubbert and Rubey, 1959]

1 which explored pore fluid pressure as an important factor for small scale hydrofracturing in
2 tectonic processes, significant efforts have been made in the development of theoretical
3 fundamentals [*Biot et al.*, 1986; *J M Cleary and Illinois State Geological Survey.*, 1958;
4 *Daneshy*, 1973; *Secor*, 1965; *Valkó and Economides*, 1995]. Apart from theoretical aspects, a
5 significant amount of analytical and numerical solutions have also been put forward by many
6 investigators to address this coupled process in a qualitative and quantitative manner [*M P*
7 *Cleary and Wong*, 1985; *Flekkøy et al.*, 2002; *Gordeyev and Zazovsky*, 1992; *Meyer*, 1986;
8 *Tzschichholz et al.*, 1994; *Yu.N.*, 1993].

9
10 Most of the previous numerical tools are built on continuum approaches and consider
11 fluid flow in fractures of simple geometry (penny-shaped elliptical or vertical cracks) using the
12 theory of linear elasticity. Much of these approaches however, lack the constitutive relationship
13 of explicit coupling between the solid and fluid being considered separately and makes strong
14 approximations upon complex flow and deformation interaction arising from brittle failure,
15 material disorder and inhomogeneity present at various scales in geo-pressurized problems.
16 Some porosity controlled models [*Boone and Ingraffea*, 1990; *Flekkøy et al.*, 2002; *Mourgues*
17 *and Cobbold*, 2003; *Olson et al.*, 2009; *Wangen*, 2002] revealed that the potential response of
18 inherent poroelastic mechanics is an important parameter in hydro-driven rock failure, where the
19 seepage forces caused by pore pressure gradients [*Engelder and Lacazette*, 1990; *Rozhko*, 2010;
20 *Rozhko et al.*, 2007] in porous rocks affect the driving stress for fracture initiation and growth.
21 Regardless of the underlying driving agent hydrofracturing is a complex process which
22 incorporates the dynamic coupling of at least three sub-processes [*Adachi et al.*, 2007]; 1)
23 Restructuring of rock skeleton upon elastic/in-elastic strain. 2) Corresponding alteration of both

1 the permeability and the interstitial fluid pressure. 3) Further mechanical deformation leading to
2 fracture propagation with concurrent variation in the pore or fracture filled fluid pressure.

3 Inspired by [Flekkøy *et al.*, 2002] we extended the work of [Koehn *et al.*, 2005] to a
4 hybrid discrete-continuum constitutive modeling approach. The scheme emphasizes the
5 evolution of rock failure in the light of underlying synergistic evolution of rock permeability
6 upon fracture growth and the consequent change in interstitial pore pressure. The hypothesis is
7 that porosity effective pore pressure diffusion along the pressure gradient is critical for the
8 formation of discrete opening mode fractures and thus may influence the propagation of
9 hydrofractures at large scale in porous rocks under controlled strain conditions.

10

11 The present paper evaluates the theoretical aspects of the numerical scheme for some
12 basic configurations to which analogue and analytical studies are present i.e., hydrofracturing in
13 homogeneous porous media under hydrostatic and non-hydrostatic conditions. In the following
14 section we give details of the fluid-solid two-way coupling scenario of the scheme. In section 3
15 the validation of the solution is given and in section 4 implementations of the method is
16 illustrated by means of simulation examples related to simple geometrical problems. Finally,
17 results from this study are pointed out in section 5. The Alternative Direction Implicit procedure
18 for the solution of the continuum diffusion is given in the Appendix-A.

19

20 **2) Formulation**

21 The simulations implemented in this study constitute of a special solution of the Darcy
22 based Navier Stoke's equation and its coupling with a discrete poroelastic medium. The basic
23 assumption is that the poroelastic feedback is behaving according to Biot's poroelastic theory

1 within a linear elastic regime. This connects pore-scale force balanced hydro-physics with the
2 evolution of the effective pressure gradient in a porous rock. Once a fracture initiates, the overall
3 behavior of the model becomes plastic and Biot's compressibility is no longer applicable
4 [Flekkøy *et al.*, 2002]. The numerical scheme can encounter the displacement of discrete
5 particles or deformation of a solid matrix directly. In this way the hydrodynamics evolve
6 intrinsically with irreversible micro deformation in a solid matrix through the use of the Kozeny-
7 Carman porosity-permeability relation.

8
9 The solution procedure adopted for this coupled problem is based on the same basic
10 principles that were successfully used in simulations to model instabilities in fluid filled granular
11 media [Johnsen *et al.*, 2006, 2007, 2008; McNamara *et al.*, 2000]. The same type of hybrid
12 models was also used to model gravitational instabilities in Rayleigh-Taylor like situations with
13 grains falling in a gas [J. L. Vinningland *et al.*, 2007a, 2007b, 2009a, 2009b, 2010], or a fluid
14 [Niebling *et al.*, 2010a, 2010b; Vinningland *et al.*, 2012], and in situations of aerofracturing, i.e.
15 injection of gas in granular media [Niebling *et al.*, 2012a, 2012b]. It was shown to reproduce
16 lubrication in sheared fault gouges due to the presence of an interstitial fluid [Goren *et al.*, 2010,
17 2011] and a variant of two fluid models is used to model fluidizes beds [Jackson, 2000] and
18 saturated landslides [Denlinger and Iverson, 2001; Spickermann *et al.*, 2012]. In the following
19 subsections we outline the idealizations employed to set up the hybrid model and describe the
20 model components along with the formulation of constitutive equations. Then we turn to the
21 solution of the fluid-solid interaction, deformation mechanism and finally the assumptions made
22 in this study.

1 **2.1) Methodology:**

2 The numerical scheme is built on a 2D hybrid Particle-Lattice model of unit dimension
3 that utilizes a small-scale triangular discrete spring network code inherited from the software
4 ‘Latte’ (part of the modeling environment ‘Elle’, [Bons *et al.*, 2007; Koehn *et al.*, 2005]) as a
5 deformation isotropic porous material. The discrete lattice is then coupled with a continuum fluid
6 phase presented by a stationary square grid of equivalent or larger dimension (figure 2).

7
8 The computation is governed by a set of two differential equations, one deals with the
9 translation (elastic deformation) of solid particles and the second solves the time dependent
10 diffusion of fluid pressure according to local strain rates through a poro-elasto-plastic
11 relationship. For a given configuration of the pressure field and the solid particles, the respective
12 constitutive equations are approximated separately by two different numerical procedures. The
13 elastic media is relaxed by a standard over-relaxation algorithm containing kinematic boundary
14 conditions ($n \cdot u = 0$) for boundary particles, while the Pressure ADI routine is used for the
15 solution of the pressure diffusion in a continuum grid (Appendix-A).

16
17 **(Figure – 2)**

18
19 With a local mass to momentum conservation, the scheme embodies coupling between
20 the solid and the Darcy continuum description. The porosity dependent evolution of the pressure
21 gradient imparts fluid drag forces at the particles of the discrete model. Permeability is treated as
22 an implicit fluid flow property and is an output of the discrete model as a function of change in

1 local porosity where the change in porosity is determined by the translational movement of mass
2 centers of the particles.

3

4 **2.2) Discrete elastic model**

5 The 2D DEM model is assembled by coupling a triangular network of volume-less linear
6 elastic springs with a particle model where disk shaped particles of constant radius superpose the
7 nodes of the triangular structure. The particle model has its genesis from molecular dynamic
8 models and represents the discrete quantities of the solid material, whereas following Hook's law
9 of interaction the spring lattice model inherits the micro-mechanical physics between the nodes.
10 This setup thus mimics isotropic elastic behavior of solid materials and can be used to model
11 deformation problems in systems described by linear elastic theory. The intrinsic stiffness
12 constant k of linear springs is related to macro-scale elastic material-parameters (E, ν) through
13 the consistency measures of strain energy between the 2-D elastic lattice of the triangular
14 network and solid continua [Flekkøy *et al.*, 2002].

$$15 \quad k = \frac{\sqrt{3}}{2} El \quad (1)$$

16 where l corresponds to the thickness of the 2D particle-lattice model.

17

18 The model produces plain strain deformation and a large-scale average stress tensor can
19 be determined from the local deformations of elastic springs for each time step Δt . Springs can
20 break when a prescribed tensile stress threshold is overcome to exhibit discrete mode-I fractures
21 in the material. Broken springs are removed from the elastic network, whereas the respective
22 particles still retain repulsive forces to accommodate the successive tension. The breaking

1 strength of springs is related to the mode-I stress intensity factor K_I , a key parameter that gives
 2 stress singularities at crack tips and does depend on the size of micro cracks in the material
 3 [*Flekkøy et al.*, 2002].

$$4 \quad K_I = \sigma_I \sqrt{\pi a} , \quad (2)$$

5 where σ_I is the critical mode-I driving stress for the relative displacement of fracture walls and
 6 a is the length of micro cracks in an isotropic medium. The porous model is assumed to be
 7 homogeneous corresponding to its elastic properties on large scale, however inherent disorder
 8 ubiquitous in natural media can be quenched through characteristic distributions of material
 9 properties on particles or annealed disorder (Griffith's micro cracks and other defects at grain
 10 scale) can be introduced by modifying the elastic properties of mechanical springs. It has been
 11 indicated that fracture patterns observed both in field and laboratory studies can be replicated by
 12 implying the realistic normal distribution of strength threshold in DEM models [*Malthe-*
 13 *Sørenssen et al.*, 1998a, 1998b; *Walmann et al.*, 1996].

14
 15 To avoid rigid body translation the elastic system is confined (closed system) by elastic
 16 walls at the boundaries. The walls behave as linear elastic springs and exercise a force on the
 17 confronted particles proportional to their distance. For instance, the force by a lateral wall on
 18 particle i contacted at $x = x_w$ is

$$19 \quad f_i = \begin{cases} -k_w(x_i + r_i - x_w)n_i & \text{if } x_i + r_i - x_w > 0 \\ 0 & \text{else} \end{cases} \quad (3)$$

20 where r_i is the particle radius, n_i is a unit vector normal to the wall and k_w is a spring constant
 21 for particle wall interaction.

22

1 2.3) 2D Pressure diffusion field

2 With negligible fluid inertia, a time dependent macroscopic diffusion equation is derived
3 that contains mass and momentum conservation in the bulk simulation of particle and continuum
4 dynamics. The output is an interstitial fluid flow expressed in terms of a porosity dependent
5 pressure gradient, which makes the computation simple and efficient. We start with the
6 continuity equations (both for solid and fluid) at a characteristic scale of a grain diameter.

$$7 \quad \partial_t [(1-\phi)\rho_s] + \nabla \cdot [(1-\phi)\rho_s u_s] = 0 \quad (4)$$

$$8 \quad \partial_t (\phi\rho_f) + \nabla \cdot (\phi\rho_f u_f) = 0 \quad (5)$$

9 where ρ_s , ρ_f are the densities and u_s , u_f the velocities of the solid particles and fluid
10 respectively and ϕ is the local porosity. The Darcy equation for the segregation of fluid and
11 solid gives a local fluid seepage u_f for a pressure drop described by the local permeability on a
12 unit area that is larger than the grain diameter.

$$13 \quad \phi(u_f - u_s) = -\frac{K}{\mu} \nabla P \quad (6)$$

14 where μ and P stand for the fluid viscosity and pressure, whereas the local permeability K is
15 expressed as a function of the local solid fraction ρ according to the empirical Kozeny-Carman
16 relation for a Darcy like regime.

$$17 \quad K(\rho) = \frac{d^2(1-\rho)^3}{180\rho^2} \quad (7)$$

18 where d is the particle diameter and 1/180 is an empirical constant valid for packing of spheres.
19 Similar to the quenched noise in elastic material constants, a distribution of hydraulic particle
20 size can be treated as an epoxy to intrinsic hydraulic heterogeneity (solid fraction, permeability)
21 in the continuum routine. In general, a larger particle area will result in low permeability and

1 high pressure gradient and eventually an overall larger fluid drag force at the local fixed scale of
 2 reference and vice versa. To get a fully consistent picture, the fluid adiabatic compressibility β
 3 is included into the continuity equation according to the fluid state equation i.e., proportional
 4 approximation of the fluid density to pressure:

$$5 \quad \rho_f = \rho_o(1 + \beta P) , \quad (8)$$

6 where ρ_o denotes the fluid density at some reference pressure. Substituting ρ_f and u_f into
 7 equation (5) and eliminate $\partial_t \phi$ from the subsequent equation we end up with the following
 8 diffusion equation for the non-hydrostatic pressure P , with an approximation of finite solid
 9 compressibility relative to fluid.

$$10 \quad \phi \beta (\partial_t P + u_s \nabla \cdot P) = \nabla \cdot \left[(1 + \beta P) \frac{K}{\mu} \nabla P \right] - (1 + \beta P) \nabla \cdot u_s . \quad (9)$$

11 The left hand side of equation (9) is the Lagrangian derivative of pore pressure, the first
 12 term on the right hand side describes the Darcy diffusion of the fluid pressure relative to particles
 13 and the third term in the equation is distinguished as source term. The source term facilitates a
 14 pressure change as a function of a change in the particle solid fraction if particles move apart in
 15 the local reference scale of Darcy flow. For a detailed dimensional and non-dimensional
 16 derivation of the continuum equation presented above see the reference [Gidaspow, 1994; Goren
 17 *et al.*, 2010, 2011].

18

19 The assumption of omitted fluid inertia is evident in equation (9), where the fluid flow is
 20 described by the pressure field $P(x, y)$ only. This diffusive-advective description of the fluid
 21 flow is valid when the Reynold's number $Re = u_f d \rho_f / \mu$ is small, where μ is dynamic viscosity

1 of the fluid, d the particle size (diameter). The Reynold's number will be small if particles are
 2 small as is in the considered cases of dense model. Assuming the validity of the current
 3 approach a priori, one can also evaluate the condition of $Re < 1$ using Darcy's law i.e.,
 4 $Re = -(Kd^{\rho_f/\mu^2})\nabla P$ in the simulations (which is true for all the cases subjected d here). As far as
 5 the particle movement (fracture aperture) is comparable to the diameter of particles, the above
 6 assumption of negligible fluid inertia is valid. However, if the fracture aperture becomes broader
 7 (sub-particle scale) the fluid inertia becomes important. This not only affects the particle-fluid
 8 coupling but also the fluid dynamics and in this case an equation describing the flow of fluid
 9 momentum, like the Navier-Stokes equation is required [McNamara *et al.*, 2000]. Nevertheless,
 10 this approach is also valid for flow fields at large Reynold's numbers [Beetstra *et al.*, 2007].

11 **2.4) Two way solid-continuum interaction**

12 The DEM lattice is blanketed over the continuum grid in a way that the boundaries of the
 13 two parallelized lattices coincide with each other. With the lattice constant of the continuum grid
 14 set to be twice as large as that of the discrete lattice, this setup incorporates the "cloud in a cell"
 15 method (figure 3) to facilitate the two-way interaction between the porous matrix and the
 16 hydrodynamic phase. The particle density ρ and velocity u are estimated locally on the
 17 continuum grid in each iteration as a function of the local mean particle density specified by a
 18 linear tent weight function upon four nearest grid nodes.

$$19 \quad \rho(r_o) = \sum_i^n s(r_i - r_o) \quad (10)$$

$$20 \quad u(r_o) = \sum_i^n u_i s(r_i - r_o) \quad (11)$$

1 where subscript i stands for particle number and the smoothing function $s(r - r_o)$ satisfies the
 2 weighted distribution of particle mass relative to its position.

$$3 \quad s(r - r_o) = \begin{cases} \left(1 - \frac{w_1}{\Delta x}\right) \left(1 - \frac{w_2}{\Delta y}\right) & \text{if } w_1 < \Delta x, w_2 < \Delta y \\ 0 & \text{otherwise} \end{cases} \quad (12)$$

4 where $r(x, y)$ and $r_o(x_o, y_o)$ are the positions of the particle and the continuum node
 5 respectively, $w_1 = |x - x_o|$ and $w_2 = |y - y_o|$ are the relative distances.

7 **(Figure – 3)**

9 With this configuration, the fluid drag force f_p on each particle encountered by a fluid
 10 continuum cell can also be deduced by averaging the pressure gradient at the respective
 11 continuum node.

$$12 \quad f_p = - \sum_k s(r_i - r_k) \left(\frac{\nabla P}{\rho_n} \right)_k \quad (13)$$

13 where k runs over four nearest grid nodes. This definition guarantees the mutual and balanced
 14 attribution of the pressure force f_p to solid particles from the continuum grid and the
 15 density/momentum contribution of the grains to the respective continuum unit cell as determined
 16 by equation (20) below.

17
 18 In the coupled scheme, fluid pressure gradients that are approximated between fixed
 19 continuum nodes produce effective stresses at the particles of the DEM lattice. This steers the
 20 particles to displace and leads to stretching of the connected elastic springs, which ultimately

1 break and be demonstrated as explicit fracturing when the imposed effective stress exceeds a
 2 given tensile stress threshold. Upon the formation of discrete cracks, rearrangement of the
 3 particles in the elastic medium (i.e., fracture opening) devise local changes in the background
 4 void space of the system, which in turn affects the permeability to be used in the successive step
 5 to determine the fluid pore pressure field. This evolution of fluid pore pressure again provides
 6 feedback to the stress field in the system and leads to fracture propagation or opening as a
 7 function of the particle dynamics. The procedure is repeated until both the continuity equation
 8 and the discrete grains are relaxed. The flowchart for one complete cycle of the algorithmic
 9 scheme is given in figure 4.

10
 11 **(Figure – 4)**

12 **2.5) Deformation mechanics**

13
 14 The translation motion of the initially relaxed solid particles (solid-solid interaction) is
 15 managed by the momentum exchange between solid and fluid phases in a unit volume cell dV
 16 (with unit third dimension) of the coupled system on account of-the inter-particle contact force
 17 f_e (either connected with a spring or repulsive force), fluid force f_p and gravity loading f_g .

$$18 \quad m \frac{dV}{dt} = f_e + f_p + f_g \quad (14)$$

19 where the forces f_e being aligned along the connected elastic springs are characterized by spring
 20 constant k_{ij} times the actual distance between the centroid of the particles minus the equilibrium
 21 distance a_{ij} .

$$22 \quad f_e = \sum_j k_{ij} (|a_{ij}| - (x_i - x_j)) \cdot \hat{n}_{ij} \quad (15)$$

1 where x_i and x_j are the positions of the connected particles, \hat{n}_{ij} is unit vector pointing from the
 2 centroid of particle i to particle j and the sum runs over all the connected neighbors j . The
 3 fluid force f_p that acts on the surface normal dA of the unit cell is a result of the fluid flow due
 4 to the pressure gradient and is given as:

$$5 \quad f_p = -\int P dA \quad (16)$$

6 where P is the local fluid pressure, which is the sum of the hydrostatic pressure $\rho_f g z$ and
 7 extraneous pressure P_o . The term gravitational force f_g incorporates the gravity effects of both
 8 the fluid and solid masses where the former together with the hydrostatic part of pressure
 9 determines the effective stress $\sigma_{eff} = (\rho_s - \rho_f) g z$ on the solid particles.

$$10 \quad f_g = \rho_s \cdot \rho dV \cdot g + \rho_f \cdot \phi dV \cdot g \quad (17)$$

11 In the geological realm a transient hydrofracturing is likely to take place by a pore
 12 pressure P in excess to σ_{eff} . However, for the considered linear elastic model that exhibits
 13 deformation in a quasi-static fashion we only need to assume pore pressure deviations from the
 14 lithostatic pressure. This has been achieved by introducing the effect of gravity in form of
 15 lithostatic stress and results in the calculated stresses minus the lithostatic pressure. The inferred
 16 gravity force on a single cylindrical particle i of volume $V_s = \pi r^2 h$ with base area $A_s = \pi r^2$,
 17 where $h = 1$ is the thickness in the third dimension is:

$$18 \quad f_i^g = \rho_s \pi R_i^2 g s \quad (18)$$

19 with

$$s = \frac{2 E_m A_m}{3 E_R A_R} \quad (19)$$

1 where ρ_s is the material mass density, $R_i = r_i \times S$ with S the dimension of the real system. E_m ,
2 E_R and A_m , A_R stand for the Young's Moduli and areas of particles in the model and the real
3 system respectively. The factor 2/3 in equation (19) is derived using the expedient strain-stress
4 relation ($\sigma_v = \frac{Ev}{(1+v)(1-2v)} \epsilon_h + \frac{E(1-v)}{(1+v)(1-2v)} \epsilon_v$) from the generalization of Hooke's law for a 2D plane
5 strain problem assuming $\nu = 1/3$ and zero lateral deformation. This is essential in order to
6 acquire a compatible one dimensional lithostatic stress $\sigma_v = \rho gh$ for the isotropic 2D linear
7 elastic solid.

8
9 By considering the local fluid velocity a rival of the local particle velocity i.e., high
10 viscous fluid and substituting the respective constitutive force terms in equation (14) one can
11 derive the following force-balance equation, which exhibits an explicit coupling between
12 granular motion and fluid flow in the unit cell ($dV = 1/\rho_n$).

$$13 \quad m_s \left[1 + \frac{\rho_f \phi}{\rho_s (1 - \phi)} \right] \frac{du_s}{dt} = F_i - \frac{\nabla P}{\rho_n} + \rho_{eff} V_s g, \quad (20)$$

14 where ρ_n is the particle number density, $\rho_{eff} = \rho_s - \rho_f$ is the effective mass density and g the
15 gravity. This is the translational equation of each individual particle dragged with velocity u_s in
16 the absence of any frictional and tangential effects. The mass m_s in the left term accounts for the
17 summation of fluid mass to each individual solid particle as a function of the local porosity to
18 particle number density ratio.

19 20 **2.6) Assumptions**

21 The assumptions made in order to keep the proposed scheme amenable are:

- 1 • The fluid-solid friction force at the surface of the solid particles is not considered,
2 therefore the pressure gradient ΔP is the only agent that produces a drag force (in the
3 direction of fluid flow) on particles.
- 4 • The fluid is considered to be purely viscous and therefore any effect like thermal
5 evolution of the fluid (a pivotal factor in the development of subsurface overpressure e.g.,
6 dehydration of sediments in intrusive zones in particular) is not taken into account.
- 7 • The locally interpolated solid fraction on the 2D continuum grid is multiplied by 2/3.
8 With this factor we obtain a good mapping of the 2D porosity on the corresponding 3D
9 equivalent (prerequisite for the 3D Kozeny-Carman permeability) with a match between
10 closed packed configurations and the empty configurations [McNamara *et al.*, 2000].
11 Without this correction the qualitative behavior is comparable but quantities like fracture
12 speed, propagation or the flux for certain pressure gradients can change by a prefactor,
13 roughly up to a factor 2.
- 14 • Analytically the Kozeny-Carman relation works as long as the solid fraction is greater
15 than zero, but a solid fraction of 0.15 or less presents a solid-fluid composite mainly as a
16 fluid and is thus inconsistent with the Kozeny-Carman relation (originally established for
17 dense granular media). We thus chose to apply a threshold to a permeability of a medium
18 with a solid fraction of 0.15 (e.g., in a broader fracture aperture). The main purpose of
19 limiting the solid fraction and hence permeability to this upper value is to allow larger
20 time steps and improve the speed of the model. Effectively, the zones of the model where
21 the permeability is equal to large values correspond to almost homogeneous pressure
22 zones. The exact value of this cutoff does not affect the pattern formation significantly, as

1 different values of the cutoff have been tested (between 0.25 and 0.05) without any
2 significant changes [Johnsen *et al.*, 2006; Jan Ludvig Vinningland *et al.*, 2007a].

3 4 **3) Model verification**

5 We first test the linearity of the porosity controlled Darcy flow field and the associated
6 pressure forces on each particle. If we consider compressible water as fluid in the pore space, the
7 evolution of seepage forces in the simulations (figure 5) validates the theoretical aspects of the
8 scheme. A reference model of unit dimension is taken as a porous rock where the solid skeleton
9 is composed of 11500 disc-shaped adhesive particles. The system is confined mechanically at all
10 boundaries whereas hydraulically it is restrained only at the side boundaries. Neglecting any
11 gravitational loading a hydraulic gradient i is established in the system by setting the bottom
12 boundary at a constant pressure input (normalized $P = 1.0$) and fixing the top boundary at 0.0
13 pressure respectively. The pressure input value is kept suitably low in order not to produce
14 fractures.

15
16 Two series of simulations are conducted to test the model by considering a homogeneous
17 (figure 5a) and a heterogeneous (figure 5b) porous rock respectively. In the heterogeneous case a
18 seal is inserted in the model. The seal is represented by a horizontal layer of low permeability
19 with a thickness of 0.1 with lower boundary at 0.2 and upper boundary at 0.3. In the test
20 simulations, initially a high pressure gradient is concentrated in the vicinity of the source
21 boundary, therefore only the intimate particles are subject to resultant seepage forces and
22 consolidate along the direction of the pressure drop. However, after 5000 time steps the pressure
23 gradient becomes linear and the fluid approaches a steady state flow condition in the

1 homogeneous model. In the heterogeneous medium a strong pressure drop develops across the
2 layer of relative low permeability. Two linear regimes develop, one below the seal with a
3 relatively steep gradient and one above the seal with a relatively gentle gradient. Consequently
4 vertical seepage forces of high contrast in magnitude are measured at the seal boundaries (figure
5 6).

6
7 **(Figure – 5)**

8
9 **(Figure – 6)**

11 **4) Model implementation**

12 In the following sections we show two different test cases to illustrate the development of hydro-
13 fractures in the model.

- 14 • Foremost, we discuss fracturing in a homogeneous medium where fractures develop
15 around a point source (fluid is injected locally) in the absence of external deformation.
16 We investigate the fracture pattern that develops as a function of fluid pressure gradients
17 under isotropic diffusion of the fluid pressure. In addition we analyze the influence of
18 changes in background porosity and study the state of stress during fracturing in detail.
19 Later, the likely influence of background non-hydrostatic stress states (i.e., uniaxial
20 vertical loading and pure shear deformation) on the growth of hydrofracture is also
21 examined.

22

- In the second set of two simulations, we advance to simulate fracture patterns due to local pressure sources in the presence of gravity and tectonic strains. In these cases we use examples where seepage forces develop due to a local increase in pore pressure caused by local perturbations in the stress state. In this case the tectonic strain conditions will control the different fracture patterns.

In each test the model starts from a fully relaxed state and is loaded in small steps afterwards. According to the boundary conditions loading includes increase of fluid pressure in the fluid lattice, vertical loading due to gravity or horizontal loading due to tectonic strains by moving the boundary walls. The mechanical and hydraulic boundary conditions vary accordingly with respect to the underlying problem to imitate laboratory and field conditions.

4.1) Point source in a homogeneous porous medium

In these simulations the fluid pressure is increased at a point source with a constant rate ($P/\Delta t$) at the centre of a homogeneous and isotropic poro-elastic domain. The model is mechanically confined and bears no-flow boundary conditions. In these simulations the hydrofracturing process shows two stages, fracture initiation and episodic fracture growth until the system reaches a steady state (Fig. 7).

The accumulation of fluid pressure at the point source generates an isotropic pressure gradient in the surrounding which contributes to the evolution of the effective stresses and deforms the porous rock elastically as a function of Biot's poro-elastic coefficient. The rock experiences micro fracturing from the concentration of stress on relatively weak rock elements.

1 The discrete fractures nucleate at the source location and tend to propagate into the undisturbed
2 region (Fig. 7a). At this stage, tension cracking accommodates the strain in the system and
3 results in stress relief and a potential local change in porosity when particles are pushed away by
4 the pressure force and fractures open. This cycle is repeated following the two-way temporal and
5 spatial feedback between hydraulic pressure field and elastic field on account of induced
6 fracturing in the porous matrix until a steady state condition is acquired and fracturing ceases.
7 The symmetry of the developing fracture pattern at the point of injection is a function of a
8 circular extension around the fluid source. The symmetric pattern validates the homogeneous
9 existence of pore pressure in the rock matrix. The seepage forces that develop due to the pressure
10 diffusion modify the force balance in the porous rock sample, which deterministically drives the
11 discrete tensile crack growth along the pressure gradient and results in a regular fracture
12 geometry.

13
14 **(Figure – 7a)**

15
16 Figure 7b shows the evolution of the effective mean stress in the model (positive mean
17 stress is extensional) as a function of time and the growth of broken bonds with time for the
18 simulation shown in figure 7a. In the first steps of the model the effective mean stress increases
19 in a non-linear fashion due to the diffusive nature of the pore fluid pressure. Once the tensile
20 strength of the material is reached the rock fractures suddenly and the stress drops significantly.
21 Subsequently the stress increases slowly, which is followed by subsequent failure events. Finally
22 fracture growth ceases and the mean stress reaches a steady state. Because the shown stress is an

1 average of a larger area in the model the fracturing continues locally even though the mean stress
2 has already reached equilibrium.

3

4

(Figure – 7b)

5

6

(Figure – 8)

7

8 Under the same fluid injection rate a quantitative comparison of the mean stresses in rock
9 samples with different background porosities is given in figure 8. The graphs in figure 8 show
10 the evolution of the effective mean stress field and the fracturing behavior of the rock as a
11 function of porosity. Rocks that inherit low porosity entail the production of high seepage forces
12 to drive tensile failure at comparable low average tensile stress. A low average stress illustrates
13 that the stress in a low porosity rock will be very localized around the point source. The stress
14 drop associated with failure of the material will be relatively large. In addition the state of stress
15 may be altered in these low porosity rocks due to friction along developing fractures (solid-solid
16 coupling), where the overall stress regime may become compressive (figure 8). Subsequently
17 small isolated shear or hybrid extension-shear fractures can develop near the end of the primary
18 dilational fractures when fracturing happens relatively early in low porosity rocks. When the
19 porosity becomes larger the initial loading of the system due to the fluid input becomes
20 successively more non-linear (Fig. 8) up to a point where the pressure just diffuses out of the
21 system without the creation of fractures.

22

1 We also simulated a number of examples (Appendix-B, Appendix-C) with the similar
2 hydraulic setup but different external boundary conditions. The developing fracture patterns
3 closely resemble the results observed experimentally by [Bruno and Nakagawa, 1991; Doe and
4 Boyce, 1989] in rock type material. The simulations manifest the effective influence of pore
5 pressure on the likelihood of tensile failure and the corresponding fracture propagation under
6 non-hydrostatic stress conditions in homogenous sedimentary rocks.

8 **4.2) Hydrofracturing in a homogeneous medium under gravity loading**

9 In the second set of simulations, we reproduce the patterns of hydrofracturing caused by a
10 local pore fluid overpressure under non-hydrostatic tectonic loadings of gravity and lateral
11 stresses and found the results consistent with [Rozhko et al., 2007]. The problem is analogous to
12 various geological systems (magmatic intrusions, hydrothermal venting, volcanoes etc.), which
13 yield a local perturbation in the effective stress field with the induction of localized pore
14 overpressure.

15
16 Figures 9 and 10 show simulations with a local point source at the bottom of the model,
17 where the former sustains a stress regime of horizontal extension and the later horizontal
18 compression. The model material is homogeneous and the gravitational loading is followed by
19 equation (18). In order to incorporate the effect of gravitational loading, the model is subjected to
20 a two-stage deformation in both cases. First, the model is let to settle under uniaxial gravitational
21 loading assuming the model is 1 km in depth with fixed side walls, a rock density of 2.5 kg/m^3 ,
22 Young modulus of 80GPa and Poisson ratio of $1/3$. This setup yields a global stress anisotropy
23 where vertical and horizontal stresses differ due to Poisson effects. Secondly, we apply a lateral

1 extension or compression with a relative small horizontal strain rate in order to have a fluid
2 dominated effective state of stress in the rock. A hydraulic anisotropy is produced in the
3 simulations by inducing a pressure drop with a zero assigned pressure at the upper boundary and
4 no flow boundary conditions at the side-walls.

5

6

(Figure – 9)

7

8

(Figure – 10)

9

10 The system that is loaded with a gravitational body force experiences buoyancy forces
11 i.e., $P = (\rho_s - \rho_f)gz$ in equation (9) with the reduction in effective stresses due to an increase in
12 local pore pressure. This gradient may lead to a quasi-static fracture propagation through parts of
13 the model.

14

15 The failure patterns illustrated in figures 9 and 10 are consistent with the different forces
16 that are applied. Fracturing nucleates in the areas where fluid pressures are high (point source at
17 the bottom of the models). The fractures propagate upwards reflecting the gravitational loading
18 of the system. The horizontal tectonic forces produce almost vertical extensional mode I crack
19 like failure when the system is extending (figure 9) and conjugate shear failure when the system
20 is under compression (figure 10). Even though the source of the fracturing is a high fluid
21 pressure in both cases the pattern that develops is strongly influenced by the heterogeneous stress
22 field due to gravity and tectonic loading. This is clearly illustrated when figure 7a is compared,

1 since figure 7a has the same fluid boundary condition with a point source as figures 9 and 10 but
2 the fracture pattern is very different in the later cases due to the external stress field.

3

4 **Discussion and conclusion**

5 Discrete fractures or instant opening of existing cracks as a function of fluid overpressure
6 drive perturbations in permeability, change the state of stress and the corresponding release of
7 strain energy on the scale of pores. In this contribution we present a hybrid numerical solution
8 based on first principles rather than on empirical constitutive relationship with ad hoc fitting
9 parameters to model natural examples of hydrofractures. First principles constitute the equation
10 of state separately for the fluid and the solid and the pore scaled forces balance to describe
11 interactions. The scheme thus combines the pertinent features of both continuum and DEM
12 descriptions, and examines the dynamic coupling between porous flow and diagenetic process
13 through fracture mechanics as a response to an applied pressure gradient across the system.

14

15 It appears likely that the interplay between the temporal and spatial evolution of the pore
16 pressure and tectonic/gravitational stresses manipulate hydro-fracturing and the corresponding
17 permeability changes. Our model shows an evolution of the deformation dependent permeability
18 illustrating that in hydro-mechanical systems permeability is a nonlinear and time dependent
19 parameter where fracturing localization is very important. The system reacts to forcing and
20 produces the permeability that it needs to allow the fluid pressure to diffuse. It has manifested
21 that small-scale diagenetic events can have adequate impact on the pressure field and in turn the
22 fracture geometry. In our model this effect is achieved by the idealized hydro-mechanical
23 constitutive relation of Kozeny-Carman permeability through a weighted interpolated function.

1 In this relation even small displacements of particles can lead to significant changes in the local
2 solid density and thus the Darcy fluid flow.

3

4 It has been perceived that several key features (flow rate upon compaction, yield surface, strain
5 softening and hardening etc.) of critical soil mechanics (CSSM) are inconsistent with the
6 observed porosity and pressure dependent deformation behavior of porous rocks [*Cuss et al.*,
7 2003; *Gerogiannopoulos and Brown*, 1978; *Ling et al.*, 2002; *Wong et al.*, 1992; *Wong et al.*,
8 1997]. Therefore, the use of Kozeny-Carman relation (originally developed for soils) for the
9 evolution of the permeability field in the presented model is justified. However, concerns may
10 rise where porosity-permeability relations deviate from the trend of the basic equation [*Zhu and*
11 *Wong*, 1997] e.g., fracturing in subsurface impermeable rocks causes enhancement in the
12 permeability in contrast to permeable rocks which bear a reduction in permeability. In this case
13 one can pursue either of the following two ways:

14 1. Use different modified forms of the permeability dependence on the porosity both for
15 ductile and brittle dominated deformation zones using the assumption of linearity
16 between porosity and log permeability with defined parametric values from experimental
17 data [*Sheldon et al.*, 2006].

18 2. When approximating the local dimension of induced fracture (aperture), a modified form
19 of the porosity-permeability relationship can be derived from the cubic law of fluid flow
20 in fractures [*Steefel and Lasaga*, 1994].

21 The simulated results validate the generality of the scheme implying that linear Darcy
22 flow has an effective factor in the process of hydrofracturing, and the results are in good

1 agreement with previously reported laboratory and field studies. The numerical scheme can
2 qualitatively replicate some typical quasi-static field examples of hydrofractures when different
3 modeling approaches are applied. Representative example problems constitute fracturing in
4 homogeneous and heterogeneous porous rocks analogous to hydraulic fracturing in pressurize
5 boreholes and natural fracture patterns due to local fluid overpressure. Simulation results
6 illustrate that the diffusion of fluid pressure is a crucial mechanism that interacts with the
7 effective stress field under different geological conditions and produces fracture geometries like
8 branching fractures at point sources, vertical and shear hydrofractures under
9 tensional/compressional tectonic settings.

10

11 The presented routine defines a fast approach both for qualitative and quantitative
12 estimation of hydro-driven deformation problems at micro scale. The method can also be used to
13 analysis large scale problems with the suitable selection of none dimensional parameters. In
14 general, gravity loading and the associated non-hydrostatic stress fields along with mechanical
15 heterogeneity in the lithology can have a vital influence over the evolution of buoyant effective
16 forces and thus the hydrofracture patterns. Therefore future work will attempt to integrate these
17 physical parameters in order to determine the appropriate geological conditions when analyzing
18 natural vein and joint networks in real reservoirs.

19

20 The presented scheme is also capable to model 3D hydrofracturing, which may have
21 more significant advantages in understanding the complex growth of fractures under the
22 influence of 3D heterogeneity and non-hydrostatic conditions. The only change required is the
23 interpolation of local mass density and velocity over a cubical unit volume of a 3D continuum

1 grid using the same assigned tent function. In the future we intend to couple the derived
 2 continuum code with a newly developed 3D next-nearest particle lattice code “Melange”
 3 [*Sachau and Koehn*, in press].

5 **Appendix-A: ADI - 2D Pressure Diffusion**

6 The ADI method is time implicit. With symmetric discretization in time i.e., between a forward
 7 and backward step, this methods is unconditionally stable and the precision is better than with a
 8 purely forward in time implicit method [*Press*, 1992].

9
 10 The two-dimensional pressure diffusion equation (9) can be rewritten as

$$11 \quad \frac{\partial P(\vec{r},t)}{\partial t} = (1 + \beta P) \frac{K(\vec{r},t)}{\beta \mu \phi(\vec{r},t)} \left[\frac{\partial^2 P(\vec{r},t)}{\partial x^2} + \frac{\partial^2 P(\vec{r},t)}{\partial y^2} \right] - \frac{1}{\beta \phi(\vec{r},t)} g(\vec{r},t) \quad (A1)$$

12 where $g(\vec{r},t)$ is the source term and \vec{r} stands for position in space. This is a second-order
 13 parabolic partial differential equation.

14
 15 Corresponding to the time and space discretization of the 2D pressure continuum using forward
 16 difference with time on the left-hand side and central difference with space on the right hand side
 17 of equation (A1).

$$18 \quad \frac{P_{i,j}^{n+\frac{1}{2}} - P_{i,j}^n}{\Delta t} = (1 + \beta P) \frac{k_{i,j}}{\beta \mu \phi_{i,j}} \left[\frac{P_{i+1,j} - 2P_{i,j} + P_{i-1,j}}{(\Delta x)^2} + \frac{P_{i,j+1} - 2P_{i,j} + P_{i,j-1}}{(\Delta y)^2} \right] - \frac{1}{\phi \beta} g_{i,j} \quad (A2)$$

19 where i, j and n are the indices in the x, y, and t directions respectively.

20

1 The main idea of the ADI method is to reduce the 2-D problem into a succession of two one-
 2 dimensional problems by proceeding one time step from n to $n+1$ in two sub-time steps (figure
 3 i). The first half-step (n to $n + \frac{1}{2}$) is taken implicitly in the x-direction and explicitly in the y-
 4 direction followed by the second half-step ($n + \frac{1}{2}$ to $n+1$) that is taken implicitly in the y-
 5 direction and explicitly in the x-direction.

6
 7 **(Figure – i)**

8
 9 Detailed differential equations in stage-1 for each j at marched time $n + \frac{1}{2}$ and the
 10 corresponding tridiagonal system of equations for the respective one-dimensional problem can
 11 be derived in form of matrix equation of dimension I:

12
$$-\alpha_{i,j}P_{i+1,j}^{n+\frac{1}{2}} + (1 + 2\alpha_{i,j})P_{i,j}^{n+\frac{1}{2}} - \alpha_{i,j}P_{i-1,j}^{n+\frac{1}{2}} = \gamma_{i,j}P_{i,j+1}^n + (1 - 2\gamma_{i,j})P_{i,j}^n + \gamma_{i,j}P_{i,j-1}^n - \frac{\Delta t}{2\phi\beta}g_{i,j} \quad (A3)$$

13
$$\begin{bmatrix} 1 & 0 & 0 & \dots & \dots & 0 \\ -\alpha_{i,j} & 1+2\alpha_{i,j} & -\alpha_{i,j} & 0 & \dots & \dots \\ 0 & \dots & \dots & \dots & \dots & 0 \\ \dots & \dots & 0 & -\alpha_{i,j} & 1+2\alpha_{i,j} & -\alpha_{i,j} \\ 0 & \dots & \dots & 0 & 0 & 1 \end{bmatrix} \begin{bmatrix} P_{0,j}^{n+\frac{1}{2}} \\ P_{1,j}^{n+\frac{1}{2}} \\ \dots \\ \dots \\ P_{I,j}^{n+\frac{1}{2}} \end{bmatrix} = \begin{bmatrix} 1 & 0 & 0 & \dots & \dots & 0 \\ \gamma_{i,j} & 1-2\gamma_{i,j} & \gamma_{i,j} & 0 & \dots & \dots \\ 0 & \dots & \dots & \dots & \dots & 0 \\ \dots & \dots & 0 & \gamma_{i,j} & 1-2\gamma_{i,j} & \gamma_{i,j} \\ 0 & \dots & \dots & 0 & 0 & 1 \end{bmatrix} \begin{bmatrix} P_{i,0}^n \\ P_{i,1}^n \\ \dots \\ \dots \\ P_{i,J}^n \end{bmatrix} - \frac{\Delta t}{2\phi\beta}g_{i,j} \quad (A4)$$

14 $i = 0, 1, \dots, I; j = 0, 1, \dots, J$

15 where

$$\alpha_{i,j} = (1 + \beta P) \frac{K_{i,j} \Delta t}{2\mu\beta\phi_{i,j}(\Delta x)^2} \quad \text{and} \quad \gamma_{i,j} = (1 + \beta P) \frac{K_{i,j} \Delta t}{2\mu\beta\phi_{i,j}(\Delta y)^2}$$

By analogy, stage-II of the ADI method for each i at time $n+1$, is expressed in tridiagonal system of dimension J :

$$-\gamma_{i,j} P_{i,j+1}^{n+\frac{1}{2}} + (1 + 2\gamma_{i,j}) P_{i,j}^{n+\frac{1}{2}} - \gamma_{i,j} P_{i,j-1}^{n+\frac{1}{2}} = \alpha_{i,j} P_{i+1,j}^n + (1 - 2\alpha_{i,j}) P_{i,j}^n + \alpha_{i,j} P_{i-1,j}^n - \frac{\Delta t}{2\phi\beta} g_{i,j} \quad (\text{A5})$$

$$\begin{bmatrix} 1 & 0 & 0 & \dots & \dots & 0 \\ -\gamma_{i,j} & 1+2\gamma_{i,j} & -\gamma_{i,j} & 0 & \dots & \dots \\ 0 & \dots & \dots & \dots & \dots & 0 \\ \dots & \dots & 0 & -\gamma_{i,j} & 1+2\gamma_{i,j} & -\gamma_{i,j} \\ 0 & \dots & \dots & 0 & 0 & 1 \end{bmatrix} \begin{bmatrix} P_{i,0}^{n+1} \\ P_{i,1}^{n+1} \\ \dots \\ P_{i,J}^{n+1} \end{bmatrix} = \begin{bmatrix} 1 & 0 & 0 & \dots & \dots & 0 \\ \alpha_{i,j} & 1-2\alpha_{i,j} & \alpha_{i,j} & 0 & \dots & \dots \\ 0 & \dots & \dots & \dots & \dots & 0 \\ \dots & \dots & 0 & \alpha_{i,j} & 1-2\alpha_{i,j} & \alpha_{i,j} \\ 0 & \dots & \dots & 0 & 0 & 1 \end{bmatrix} \begin{bmatrix} P_{0,j}^{n+\frac{1}{2}} \\ P_{1,j}^{n+\frac{1}{2}} \\ \dots \\ P_{I,j}^{n+\frac{1}{2}} \end{bmatrix} - \frac{\Delta t}{2\phi\beta} g_{i,j} \quad (\text{A6})$$

$$i = 0, 1, \dots, I; j = 0, 1, \dots, J$$

Implementing the Gauss-algorithm with a Dirichlet boundary condition, the derived tridiagonal system of equation (A4) is solved J times and equation (A6) by I times.

Acknowledgement:

We are deeply grateful to Till Sachau for his valuable discussions. This study was carried out within the framework of DGMK (German Society for Petroleum and Coal Science and Technology) research project 718 "Mineral Vein Dynamics Modelling", which is funded by the companies ExxonMobil Production Deutschland GmbH, GDF SUEZ E&P Deutschland GmbH, RWE Dea AG and Wintershall Holding GmbH, within the basic research program of the WEG

1 Wirtschaftsverband Erdöl- und Erdgasgewinnung e.V. We thank the companies for their
2 financial support and their permission to publish these results.

3

4 **References**

- 5 Adachi, J., E. Siebrits, A. Peirce, and J. Desroches (2007), Computer simulation of hydraulic fractures,
6 *International Journal of Rock Mechanics and Mining Sciences*, 44(5), 739-757.
- 7 Beetstra, R., M. A. van der Hoef, and J. A. M. Kuipers (2007), Drag force of intermediate Reynolds
8 number flow past mono- and bidisperse arrays of spheres, *AIChE Journal*, 53(2), 489-501.
- 9 Biot, M. A., L. Masse, and W. L. Medlin (1986), A Two-Dimensional Theory of Fracture Propagation, *SPE*
10 *Production Engineering*, 1(1), 17-30.
- 11 Bons, P. D., D. Koehn, and M. W. Jessell (2007), *Microdynamics Simulation*, Springer.
- 12 Boone, T. J., and A. R. Ingraffea (1990), A numerical procedure for simulation of hydraulically-driven
13 fracture propagation in poroelastic media, *International Journal for Numerical and Analytical Methods in*
14 *Geomechanics*, 14(1), 27-47.
- 15 Bruno, M. S., and F. M. Nakagawa (1991), Pore pressure influence on tensile fracture propagation in
16 sedimentary rock, *International Journal of Rock Mechanics and Mining Sciences & Geomechanics*
17 *Abstracts*, 28(4), 261-273.
- 18 Cleary, J. M., and Illinois State Geological Survey. (1958), *Hydraulic fracture theory*, [s.n.], Urbana.
- 19 Cleary, M. P., and S. K. Wong (1985), Numerical simulation of unsteady fluid flow and propagation of a
20 circular hydraulic fracture, *International Journal for Numerical and Analytical Methods in Geomechanics*,
21 9(1), 1-14.
- 22 Cuss, R. J., E. H. Rutter, and R. F. Holloway (2003), The application of critical state soil mechanics to the
23 mechanical behaviour of porous sandstones, *International Journal of Rock Mechanics and Mining*
24 *Sciences*, 40(6), 847-862.
- 25 Daneshy, A. A. (1973), On the Design of Vertical Hydraulic Fractures, *SPE Journal of Petroleum*
26 *Technology*, 25(1), 83-97.
- 27 Denlinger, R. P., and R. M. Iverson (2001), Flow of variably fluidized granular masses across three-
28 dimensional terrain 2. Numerical predictions and experimental tests, *J. Geophys. Res.*, 106(B1), 553-566.
- 29 Doe, T. W., and G. Boyce (1989), Orientation of hydraulic fractures in salt under hydrostatic and non-
30 hydrostatic stresses, *International Journal of Rock Mechanics and Mining Sciences & Geomechanics*
31 *Abstracts*, 26(6), 605-611.
- 32 Engelder, T., and A. Lacazette (1990), Natural hydraulic fracturing, paper presented at Rock Joints:
33 Proceedings of the international symposium on rock joints, A.A. Balkema, Rotterdam, Loen, Norway.
- 34 Flekkøy, E. G., A. Malthe-Sorensen, and B. Jamtveit (2002), Modeling hydrofracture, *J Geophys Res-Sol*
35 *Ea*, 107(B8).
- 36 Fyfe, W. S., N. J. Price, and A. B. Thompson (1978), *Fluids in the earth's crust: their significance in*
37 *metamorphic, tectonic, and chemical transport processes*, Elsevier Scientific Pub. Co.
- 38 Gerogiannopoulos, N. G., and E. T. Brown (1978), The critical state concept applied to rock, *International*
39 *Journal of Rock Mechanics and Mining Sciences & Geomechanics Abstracts*, 15(1), 1-10.
- 40 Gidaspow, D. (1994), *Multiphase Flow and Fluidization: Continuum and Kinetic Theory Descriptions*,
41 Academic Press.
- 42 Gordeyev, Y. N., and A. F. Zazovsky (1992), Self-similar solution for deep-penetrating hydraulic fracture
43 propagation, *Transport in Porous Media*, 7(3), 283-304.

1 Goren, L., E. Aharonov, D. Sparks, and R. Toussaint (2010), Pore pressure evolution in deforming
2 granular material: A general formulation and the infinitely stiff approximation, *J. Geophys. Res.*, *115*(B9),
3 B09216.

4 Goren, L., E. Aharonov, D. Sparks, and R. Toussaint (2011), The Mechanical Coupling of Fluid-Filled
5 Granular Material Under Shear, *Pure and Applied Geophysics*, *168*(12), 2289-2323.

6 Hubbert, M. K., and D. G. Willis (1957), Mechanics Of Hydraulic Fracturing *Petroleum Transactions*,
7 *AIME*, *210*, 153-168.

8 Hubbert, M. K., and W. W. Rubey (1959), Role Of Fluid Pressure In Mechanics Of Overthrust Faulting: I.
9 Mechanics of Fluid-Filled Porous Solids And Its Application To Overthrust Faulting, *Geological Society of*
10 *America Bulletin*, *70*(2), 115-166.

11 Jackson, R. (2000), *The Dynamics of Fluidized Particles*, Cambridge University Press.

12 Johnsen, R. Toussaint, K. J. Måløy, and E. G. Flekkøy (2006), Pattern formation during air injection into
13 granular materials confined in a circular Hele-Shaw cell, *Physical Review E*, *74*(1), 011301.

14 Johnsen, R. Toussaint, K. J. Måløy, E. G. Flekkøy, and J. Schmittbuhl (2007), Coupled air/granular flow in
15 a linear Hele-Shaw cell, *Physical Review E*, *77*(1), 011301.

16 Johnsen, C. Chevalier, A. Lindner, R. Toussaint, E. Clement, K. J. Maloy, E. G. Flekkoy, and J. Schmittbuhl
17 (2008), Decompaction and fluidization of a saturated and confined granular medium by injection of a
18 viscous liquid or gas, *Phys Rev E Stat Nonlin Soft Matter Phys*, *78*(5 Pt 1), 6.

19 Koehn, D., J. Arnold, and C. W. Passchier (2005), Fracture and vein patterns as indicators of deformation
20 history: a numerical study, *Geological Society, London, Special Publications*, *243*(1), 11-24.

21 Ling, H., D. Yue, V. Kaliakin, and N. Themelis (2002), Anisotropic Elastoplastic Bounding Surface Model
22 for Cohesive Soils, *Journal of Engineering Mechanics*, *128*(7), 748-758.

23 Malthe-Sørenssen, A., T. Walmann, B. Jamtveit, J. Feder, and T. Jøssang (1998a), Modeling and
24 characterization of fracture patterns in the Vatnajökull glacier, *Geology*, *26*(10), 931-934.

25 Malthe-Sørenssen, A., T. Walmann, J. Feder, T. Jøssang, P. Meakin, and H. H. Hardy (1998b), Simulation
26 of extensional clay fractures, *Physical Review E*, *58*(5), 5548-5564.

27 McNamara, S., E. G. Flekkøy, and K. J. Måløy (2000), Grains and gas flow: Molecular dynamics with
28 hydrodynamic interactions, *Physical Review E*, *61*(4), 4054-4059.

29 Meyer, B. R. (1986), Design Formulae for 2-D and 3-D Vertical Hydraulic Fractures: Model Comparison
30 and Parametric Studies, in *SPE Unconventional Gas Technology Symposium*, edited, 1986 Copyright 1986
31 Society of Petroleum Engineers, Inc., Louisville, Kentucky.

32 Mourgues, R., and P. R. Cobbold (2003), Some tectonic consequences of fluid overpressures and
33 seepage forces as demonstrated by sandbox modelling, *Tectonophysics*, *376*(1-2), 75-97.

34 Niebling, M. J., E. G. Flekkoy, K. J. Maloy, and R. Toussaint (2010a), Mixing of a granular layer falling
35 through a fluid, *Phys Rev E Stat Nonlin Soft Matter Phys*, *82*(1 Pt 1), 7.

36 Niebling, M. J., E. G. Flekkøy, K. J. Måløy, and R. Toussaint (2010b), Sedimentation instabilities: Impact of
37 the fluid compressibility and viscosity, *Physical Review E*, *82*(5), 051302.

38 Niebling, M. J., R. Toussaint, E. G. Flekkøy, and K. J. Måløy (2012a), Dynamic aerofracture of dense
39 granular packings, *Physical Review E (submitted)*.

40 Niebling, M. J., R. Toussaint, E. G. Flekkøy, and K. J. Måløy (2012b), Numerical studies of aerofractures in
41 porous media, *Revista Cubana de Fisica (submitted)*.

42 Olson, J. E., S. E. Laubach, and R. H. Lander (2009), Natural fracture characterization in tight gas
43 sandstones: Integrating mechanics and diagenesis, *AAPG Bulletin*, *93*(11), 1535-1549.

44 Press, W. H. (1992), *Numerical recipes in C: the art of scientific computing*, Cambridge University Press.

45 Rozhko, A. Y. (2010), Role of seepage forces on seismicity triggering, *J Geophys Res-Sol Ea*, *115*.

46 Rozhko, A. Y., Y. Y. Podladchikov, and F. Renard (2007), Failure patterns caused by localized rise in pore-
47 fluid overpressure and effective strength of rocks, *Geophys. Res. Lett.*, *34*(22), L22304.

1 Sachau, T., and D. Koehn (in press), 'Melange': A viscoelastic lattice-particle model applicable to the
2 lithosphere, *Geochemistry Geophysics Geosystems*.
3 Secor, D. T. (1965), Role of fluid pressure in jointing, *Am J Sci*, 263(8), 633-646.
4 Sheldon, H. A., A. C. Barnicoat, and A. Ord (2006), Numerical modelling of faulting and fluid flow in
5 porous rocks: An approach based on critical state soil mechanics, *J Struct Geol*, 28(8), 1468-1482.
6 Spickermann, A., R. Toussaint, J. Travelletti, J. P. Malet, and T. W. J. Van Asch (2012), A grain-fluid
7 mixture model to characterize the dynamics of active landslides in fine-grained soils, *J Geophys Res-Sol*
8 *Ea*.
9 Steefel, C. I., and A. C. Lasaga (1994), A coupled model for transport of multiple chemical species and
10 kinetic precipitation/dissolution reactions with application to reactive flow in single phase hydrothermal
11 systems, *Am J Sci*, 294(5), 529-592.
12 Tzschichholz, F., H. J. Herrmann, H. E. Roman, and M. Pfuff (1994), Beam model for hydraulic fracturing,
13 *Physical Review B*, 49(10), 7056-7059.
14 Valkó, P., and M. J. Economides (1995), *Hydraulic fracture mechanics*, Wiley.
15 Vinningland, J. L., Ø. Johnsen, E. G. Flekkoy, R. Toussaint, and K. J. Maloy (2007a), Experiments and
16 simulations of a gravitational granular flow instability, *Phys Rev E Stat Nonlin Soft Matter Phys*, 76(5 Pt
17 1), 27.
18 Vinningland, J. L., Ø. Johnsen, E. G. Flekkøy, R. Toussaint, and K. J. Måløy (2007a), Experiments and
19 simulations of a gravitational granular flow instability, *Physical Review E*, 76(5), 051306.
20 Vinningland, J. L., Ø. Johnsen, E. G. Flekkøy, R. Toussaint, and K. J. Måløy (2007b), Granular Rayleigh-
21 Taylor Instability: Experiments and Simulations, *Physical Review Letters*, 99(4), 048001.
22 Vinningland, J. L., Ø. Johnsen, E. G. Flekkoy, R. Toussaint, and K. J. Maloy (2009a), Granular Rayleigh-
23 Taylor instability, paper presented at 6th international conference on micromechanics of granular
24 media, powder and grains, AIP.
25 Vinningland, J. L., Ø. Johnsen, E. G. Flekkoy, R. Toussaint, and K. J. Maloy (2009b), Granular Rayleigh
26 Taylor instability, paper presented at Traffic and Granular Flow conference 2007, Orsay, 2009.
27 Vinningland, J. L., Ø. Johnsen, E. G. Flekkøy, R. Toussaint, and K. J. Måløy (2010), Size invariance of the
28 granular Rayleigh-Taylor instability, *Physical Review E*, 81(4), 041308.
29 Vinningland, J. L., R. Toussaint, M. Niebling, E. Flekkøy, and K. Måløy (2012), Family-Vicsek scaling of
30 detachment fronts in granular Rayleigh-Taylor instabilities during sedimentating granular/fluid flows,
31 *The European Physical Journal - Special Topics*, 204(1), 27-40.
32 Walmann, T., A. Malthe-Sørensen, J. Feder, T. Jøssang, P. Meakin, and H. H. Hardy (1996), Scaling
33 Relations for the Lengths and Widths of Fractures, *Physical Review Letters*, 77(27), 5393-5396.
34 Wang, T.-Y., and C. C.-P. Chen (2001), Thermal-ADI: a linear-time chip-level dynamic thermal simulation
35 algorithm based on alternating-direction-implicit (ADI) method, in *Proceedings of the 2001 international*
36 *symposium on Physical design*, edited, pp. 238-243, ACM, Sonoma, California, United States.
37 Wangen, M. (2002), Effective permeability of hydrofractured sedimentary rocks, in *Norwegian*
38 *Petroleum Society Special Publications*, edited by G. K. Andreas and H. Robert, pp. 61-74, Elsevier.
39 Wong, T.-f., H. Szeto, and J. Zhang (1992), Effect of Loading Path and Porosity on the Failure Mode of
40 Porous Rocks, *Applied Mechanics Reviews*, 45(8), 281-293.
41 Wong, T.-f., C. David, and W. Zhu (1997), The transition from brittle faulting to cataclastic flow in porous
42 sandstones: Mechanical deformation, *J. Geophys. Res.*, 102(B2), 3009-3025.
43 Yu, N, G. (1993), Growth of a crack produced by hydraulic fracture in a poroelastic medium, *International*
44 *Journal of Rock Mechanics and Mining Sciences & Geomechanics Abstracts*, 30(3), 233-238.
45 Zhu, W., and T.-f. Wong (1997), The transition from brittle faulting to cataclastic flow: Permeability
46 evolution, *J. Geophys. Res.*, 102(B2), 3027-3041.

1
2
3
4
5
6
7
8
9
10
11
12
13
14
15
16
17
18
19

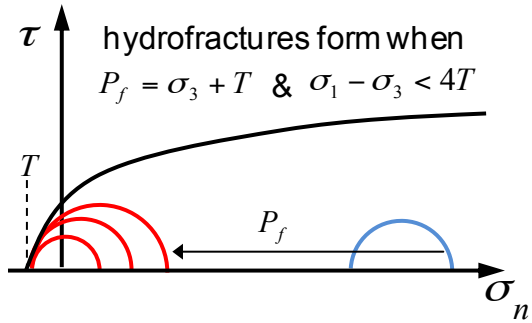
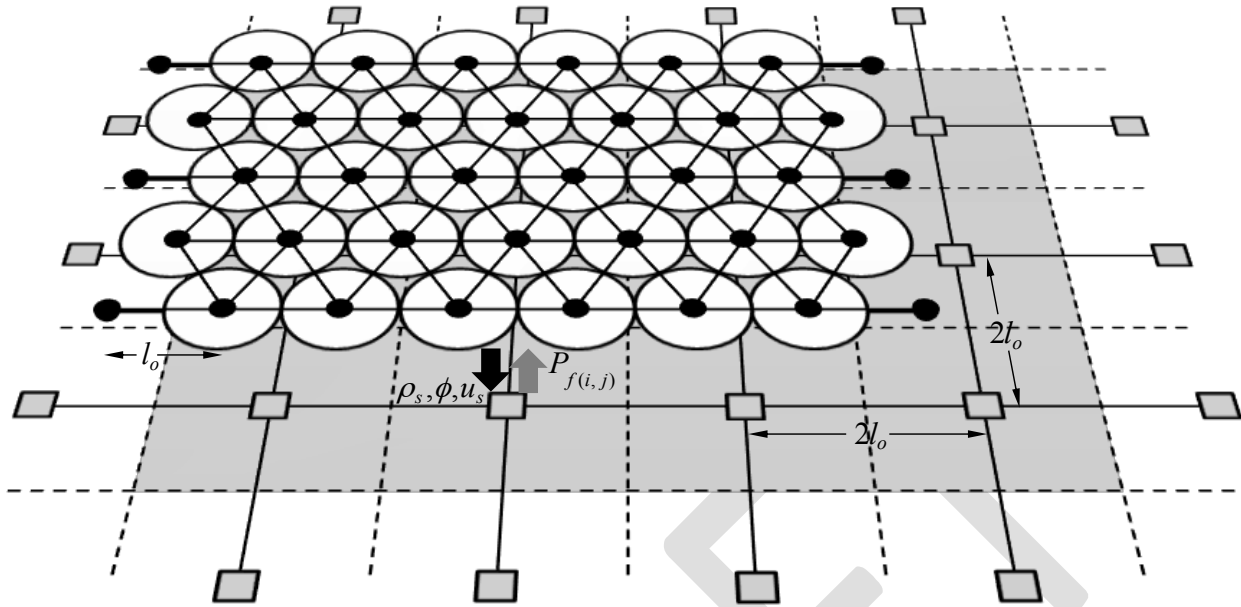


Fig. 1: Mohr diagram of tensile failure due to fluid overpressure. The blue Mohr circle represents the initial state of stress with zero fluid pressure. The Mohr circle moves towards the left hand side (red circles) as a result of fluid overpressure, which results in tensile/shear failure.

DRAFT

1



2

3 **Fig 2.** Schematic diagram of the hybrid hydro-elastic model, illustrates overlapping regions in
4 physical space comprising the DEM lattice and the continuum grid.

5

6

7

8

9

10

11

12

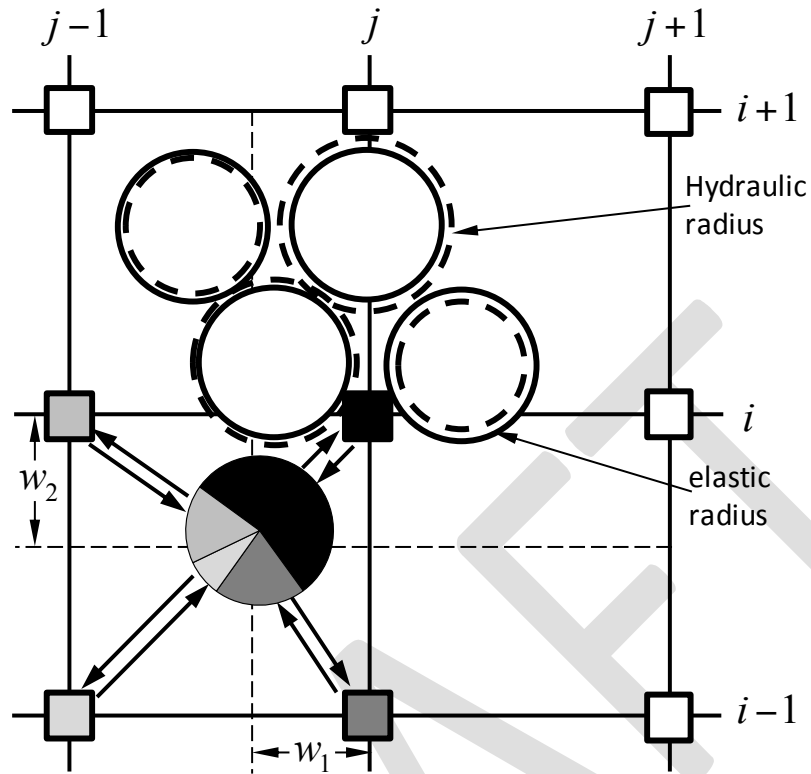
13

14

15

16

1



2

3 **Fig. 3.** General overview of the twofold function of the numerical setup. Polar arrows illustrate
4 the linear interpolation of particle area weight (grayish color code) to surrounding grid nodes and
5 in turn the time dependent drag force from grid nodes to encountered particles.

6

7

8

9

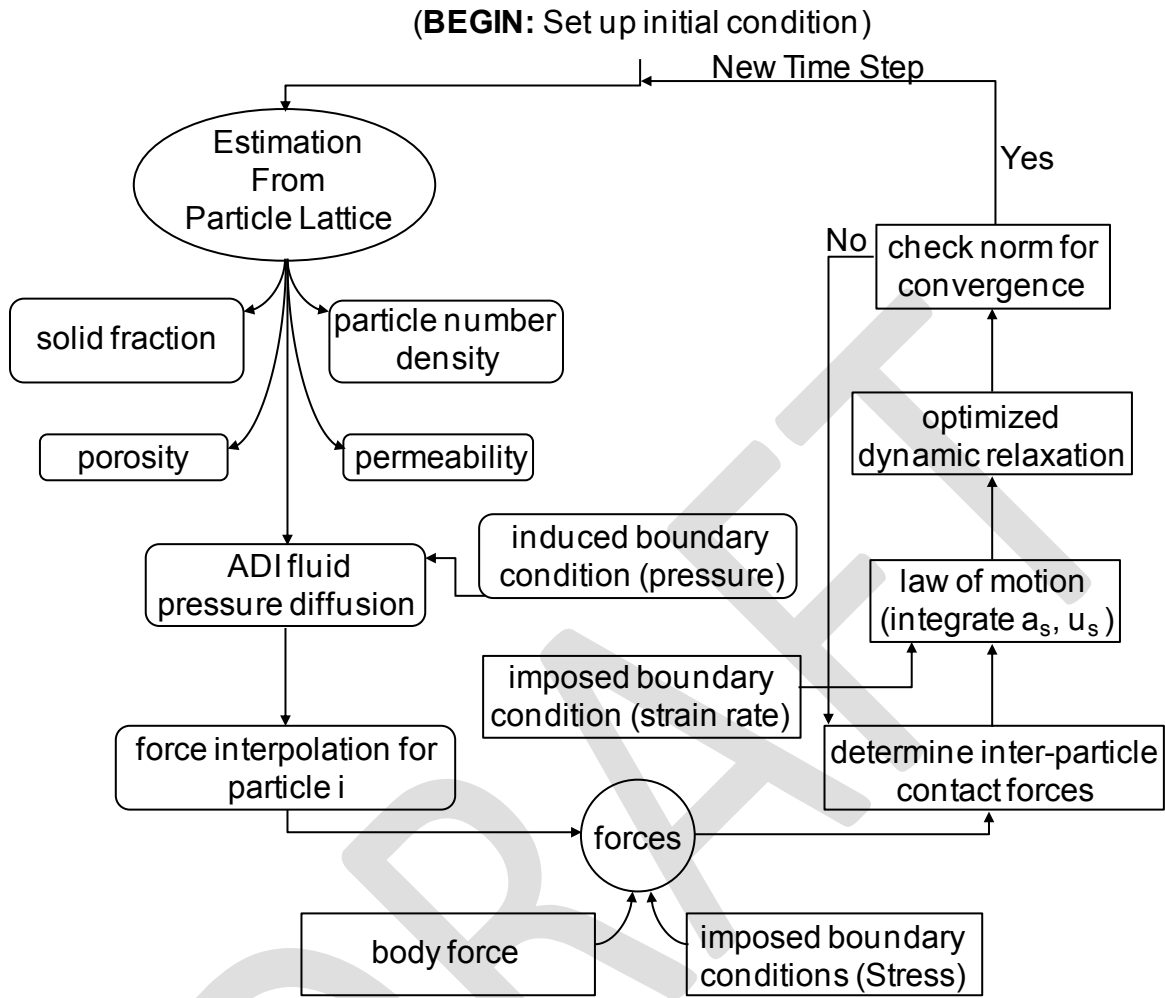
10

11

12

13

1



2

3 **Fig. 4.** Flowchart for the complete cycle of the algorithmic scheme.

4

5

6

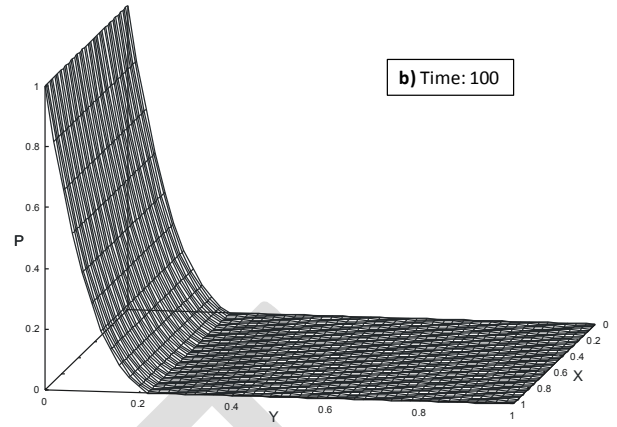
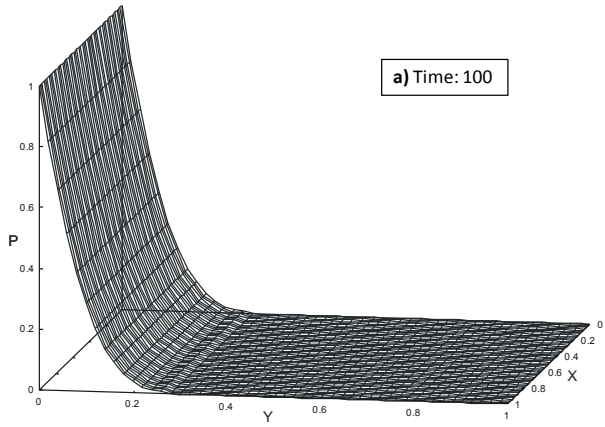
7

8

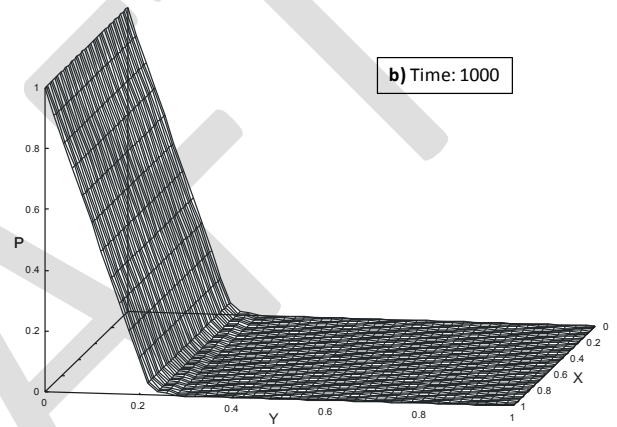
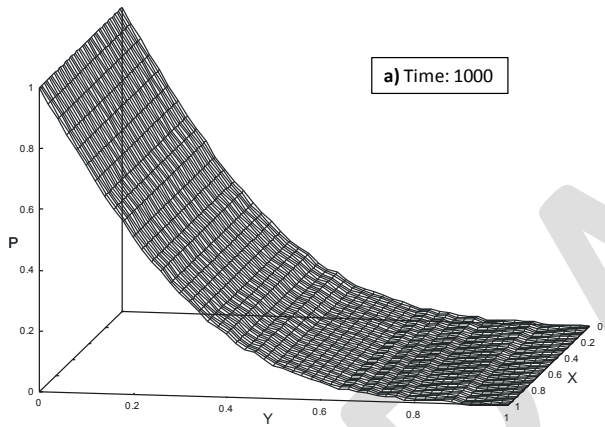
9

10

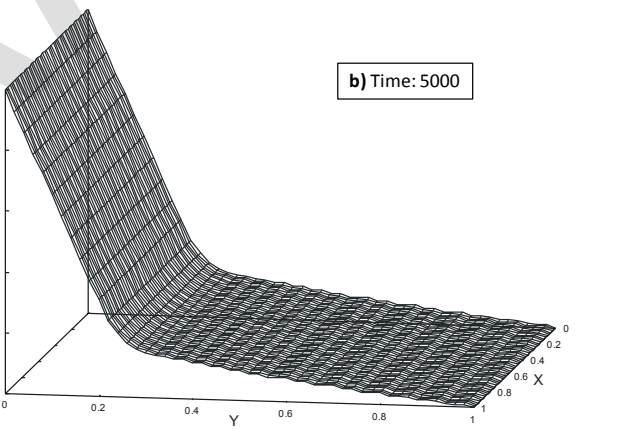
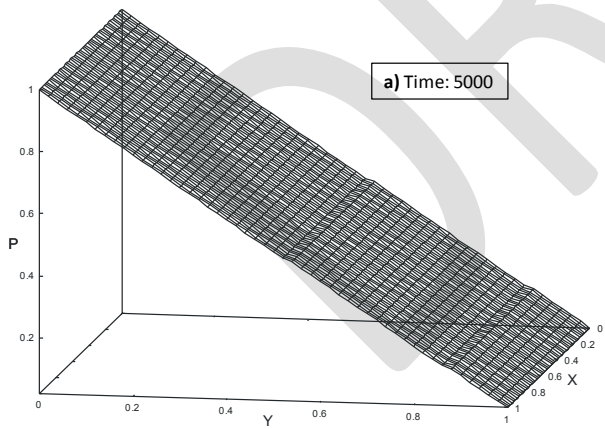
1



2



3

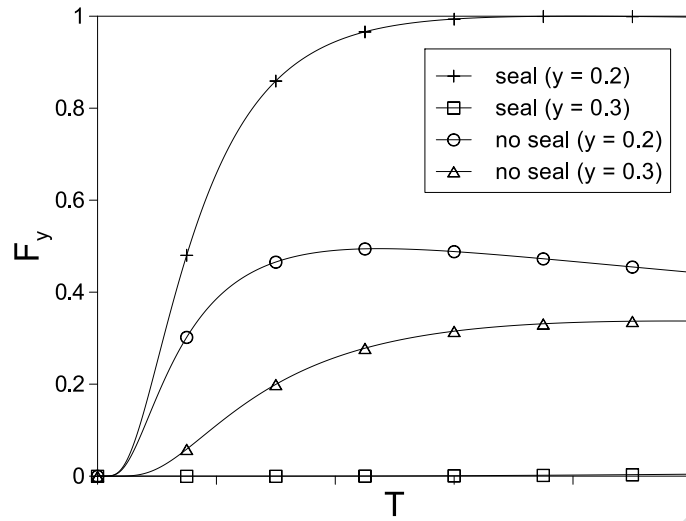


4

5 **Fig. 5.** Normalized pore pressure profiles at different time steps, (a) in a homogeneous porous
6 medium, (b) in a heterogeneous porous medium accompanying a horizontal seal of low porosity
7 at position 0.2 – 0.3 on the y-axis (vertical axis).

8

1



2

3 **Fig. 6.** Overall evolution of the vertical seepage forces as a function of time ($T:1000$) for a
4 homogeneous system and at the lower and upper boundary contacts of the seal in a
5 heterogeneous system. The forces display a sharp contrast in magnitude in the heterogeneous
6 case, whereas in the homogeneous medium the forces show a gradual increase in pressure force.
7 Both the heterogeneous and homogeneous cases reach a steady state condition.

8

9

10

11

12

13

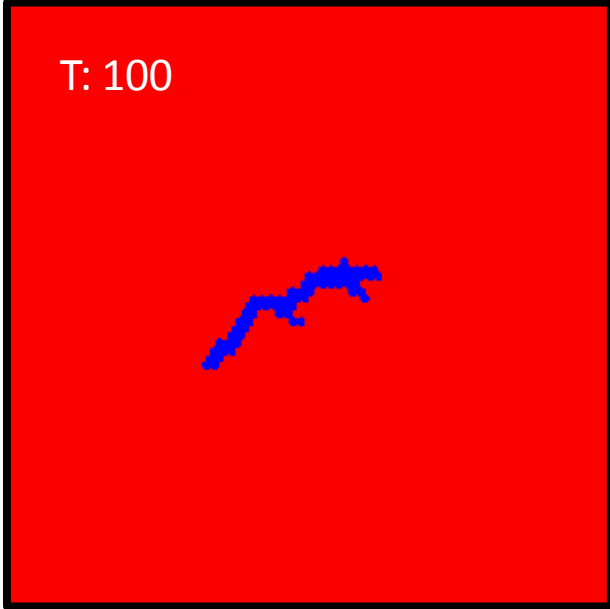
14

15

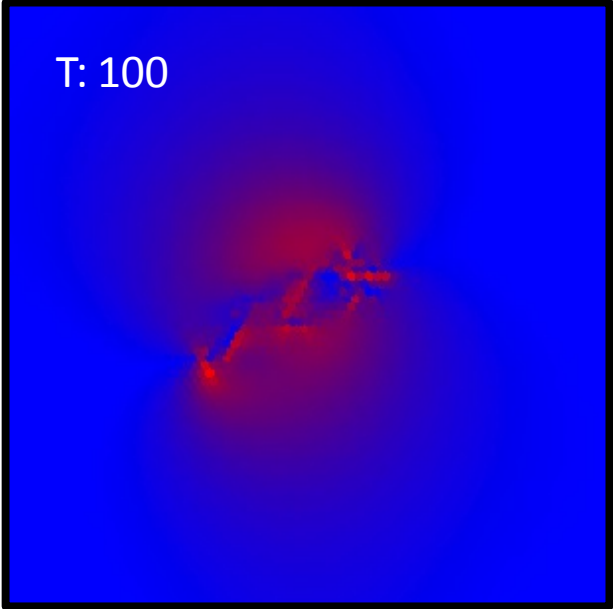
16

17

T: 100

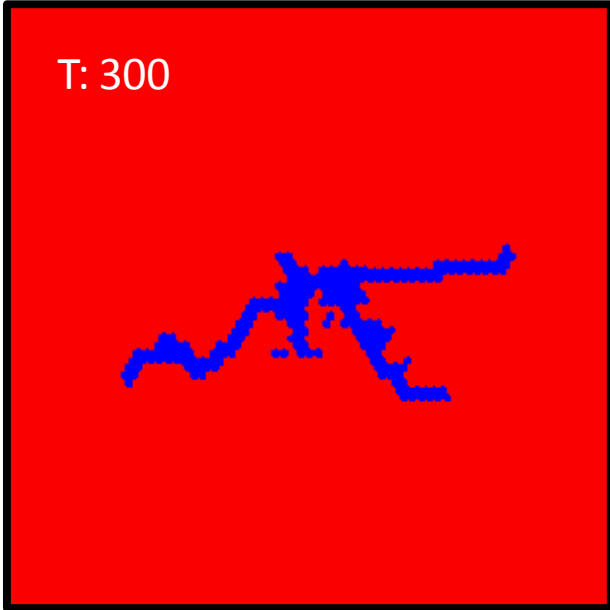


T: 100

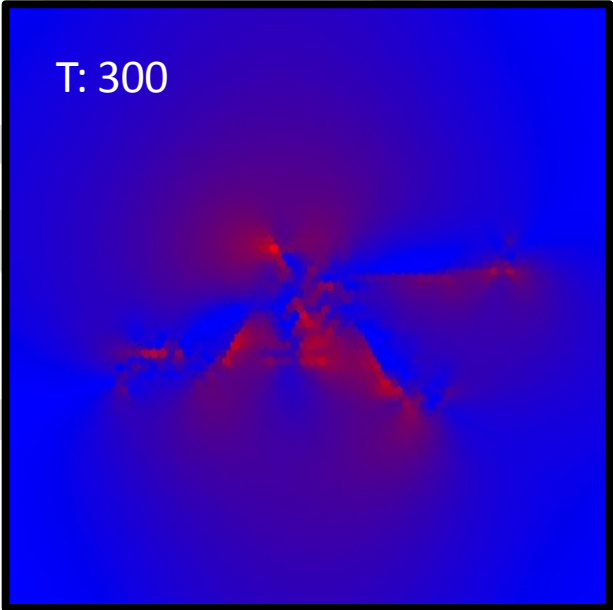


1

T: 300

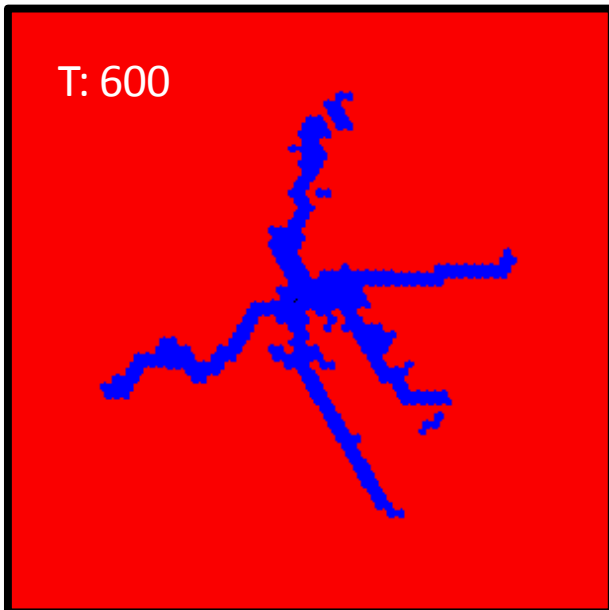


T: 300

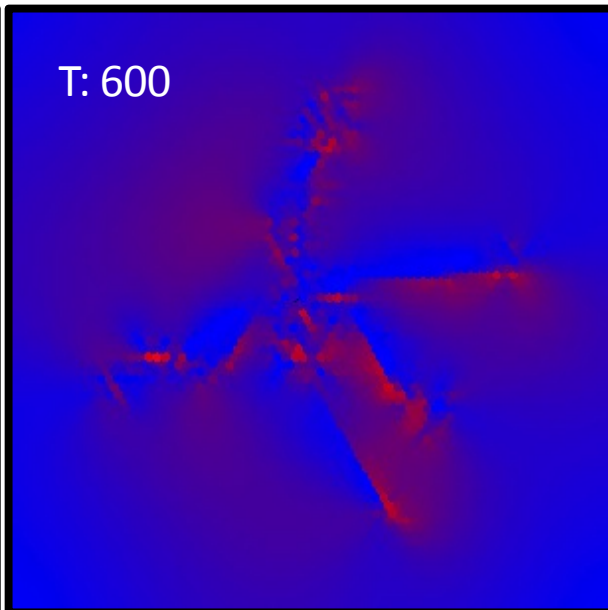


2

T: 600

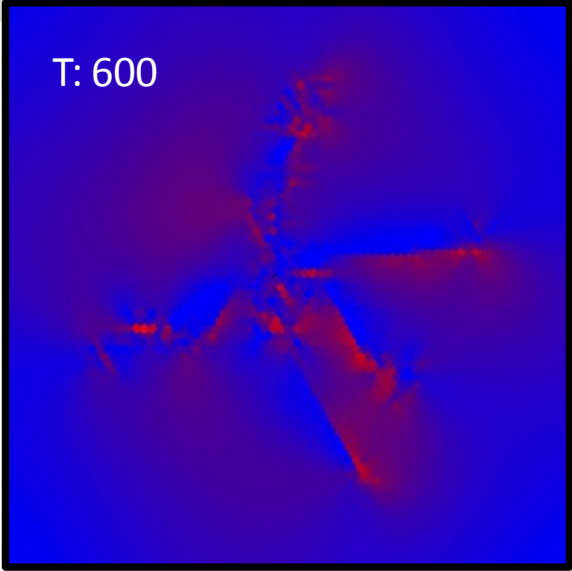
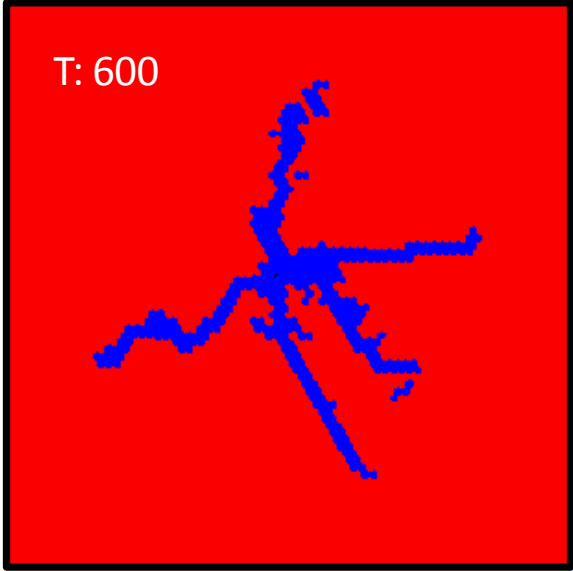
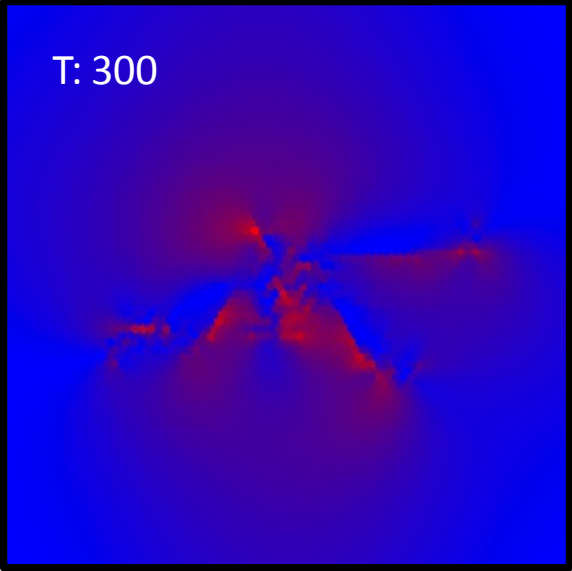
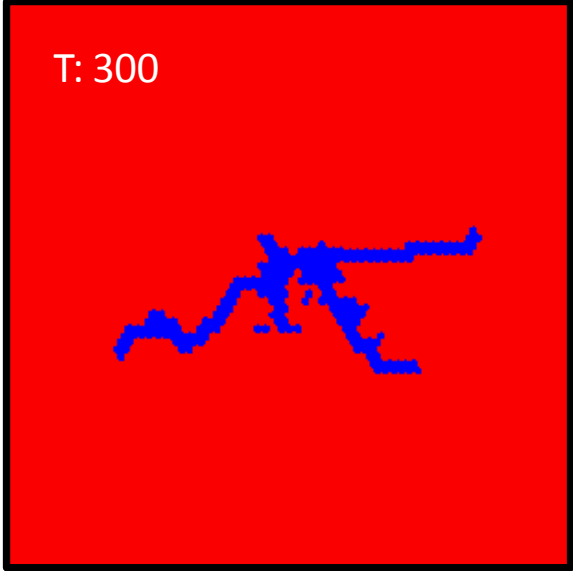
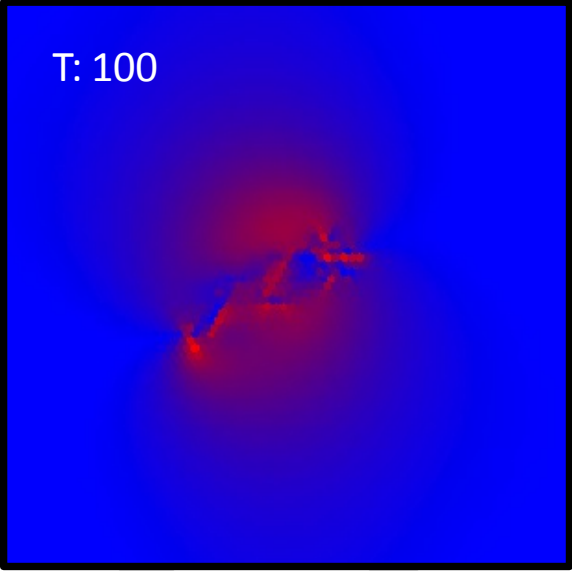
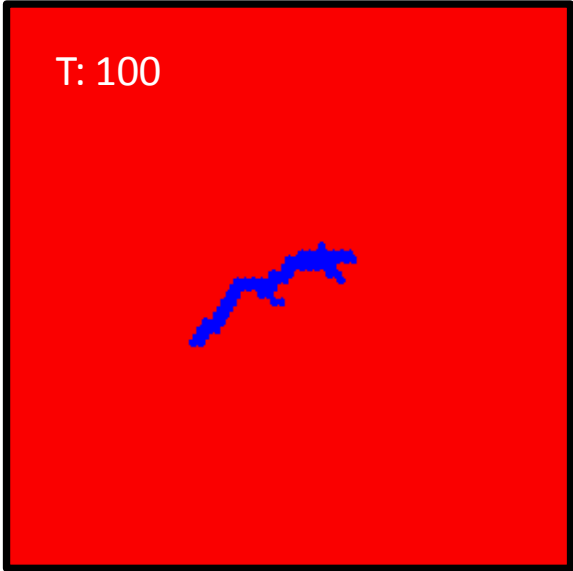


T: 600



1

DRAFT



1 **Fig. 7a.** The figures on the left hand side show the development of circular hydro-fractures (T=
2 model time, blue particles have broken bonds) by a point source overpressure. The figures on the
3 right hand side show the same simulations and illustrate the associated differential stress states of
4 the model at the respective failure stages (red=high; blue=low differential stress).

5

6

7

8

9

10

11

12

13

14

15

16

17

18

19

20

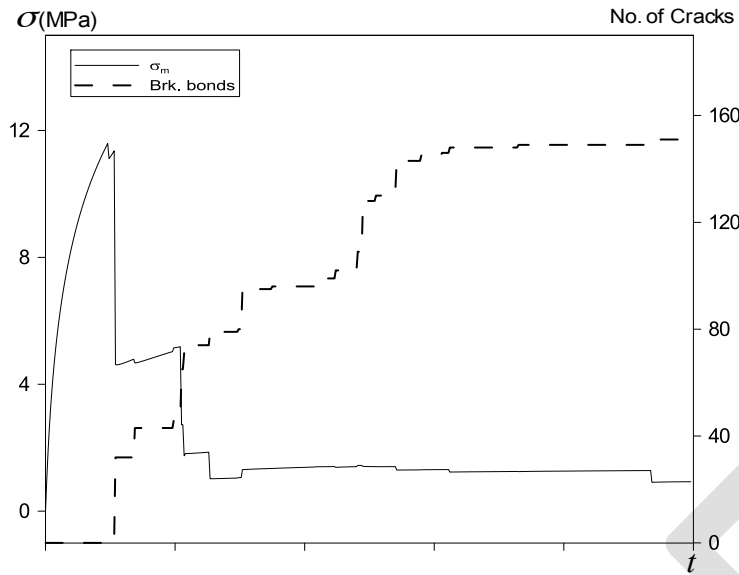
21

22

23

DRAFT

1



2

3 **Fig. 7b.** Graph shows oscillations in effective mean stress and associated number of broken
4 bonds in the model. The stress shows the episodic evolution of the fluid pressure. Positive
5 effective mean stress in the model is defined as extensional stress.

6

7

8

9

10

11

12

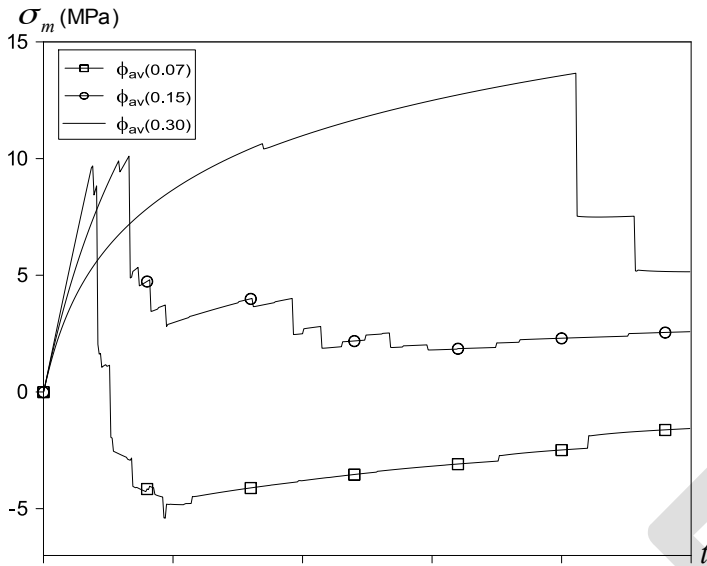
13

14

15

16

1



2

3 **Fig. 8.** Mean stress as a function of background rock porosity, where an increase in porosity
4 results in a lower driving force because the pressure can diffuse faster. Note: -ve sign in the
5 model is annotated for compressive stress and +ve sign for extensional stress.

6

7

8

9

10

11

12

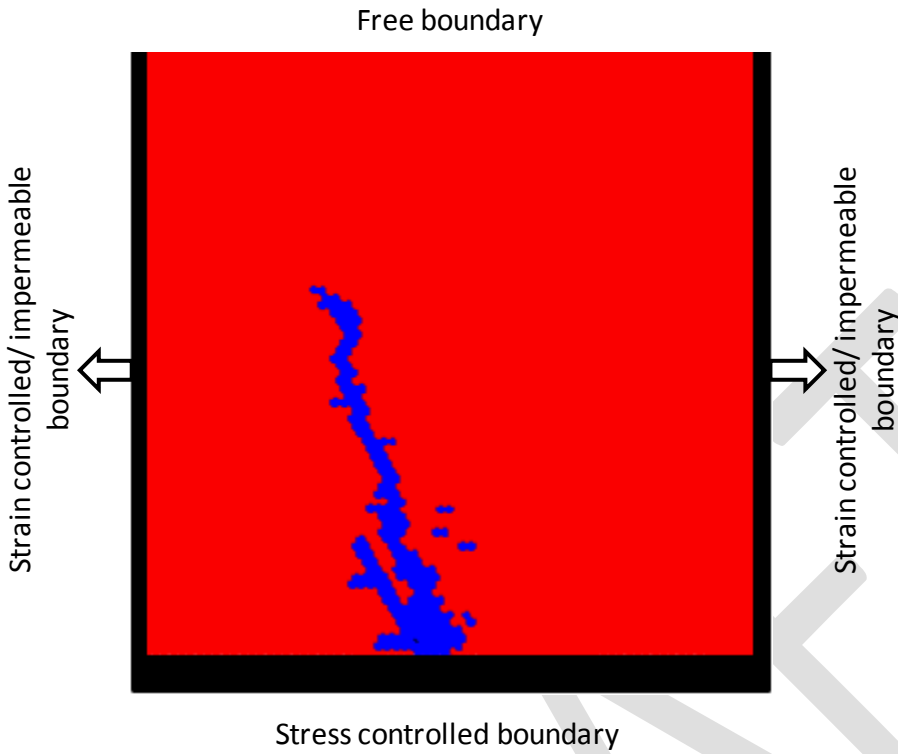
13

14

15

16

1



2

3 **Fig. 9.** Vertical hydrofracture in a rock model subjected to lateral extensional strain. A vertical
4 gravitational load is applied to the system and fluid is injected at a point source in the middle of
5 the system at the lower boundary.

6

7

8

9

10

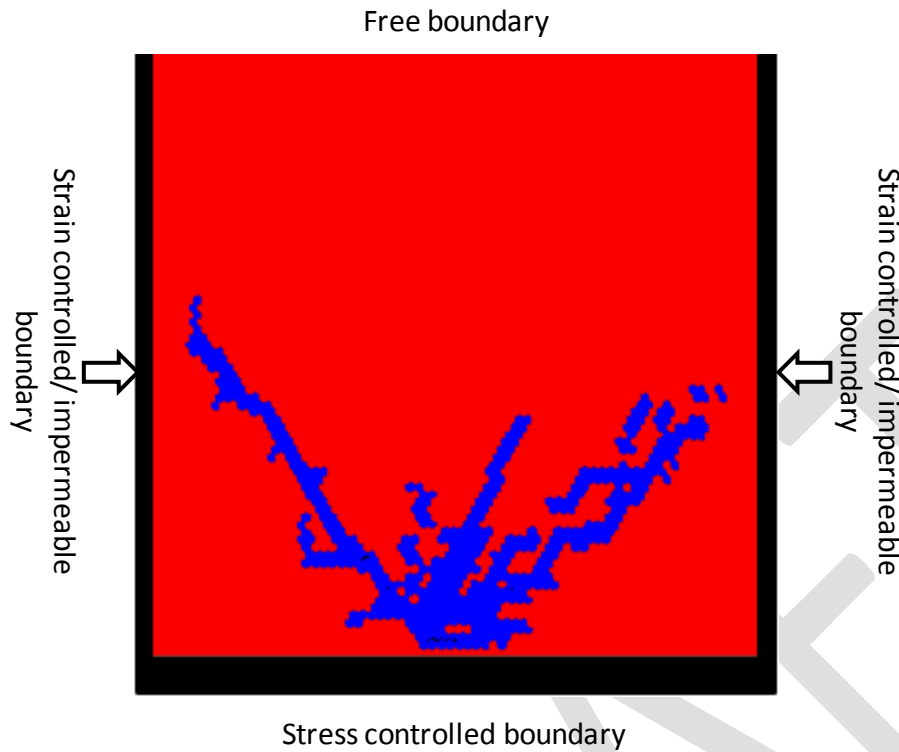
11

12

13

14

1



2

3 **Fig. 10.** Conjugate shear fractures under compressive state of stress. A vertical gravitational load
4 is applied to the system and fluid is injected at a point source in the middle of the system at the
5 lower boundary.

6

7

8

9

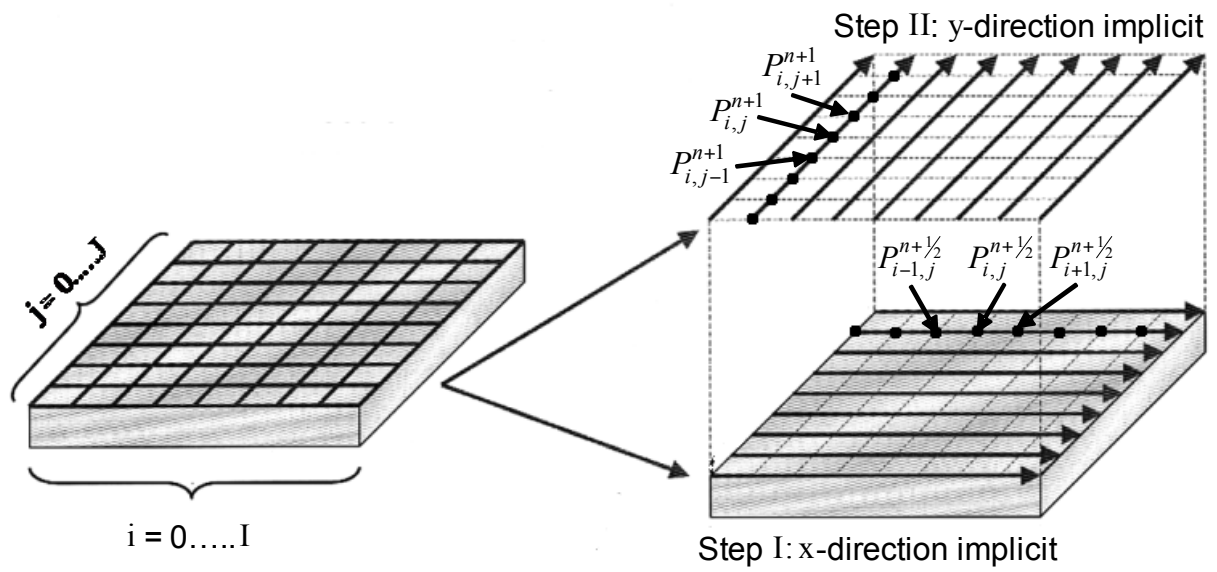
10

11

12

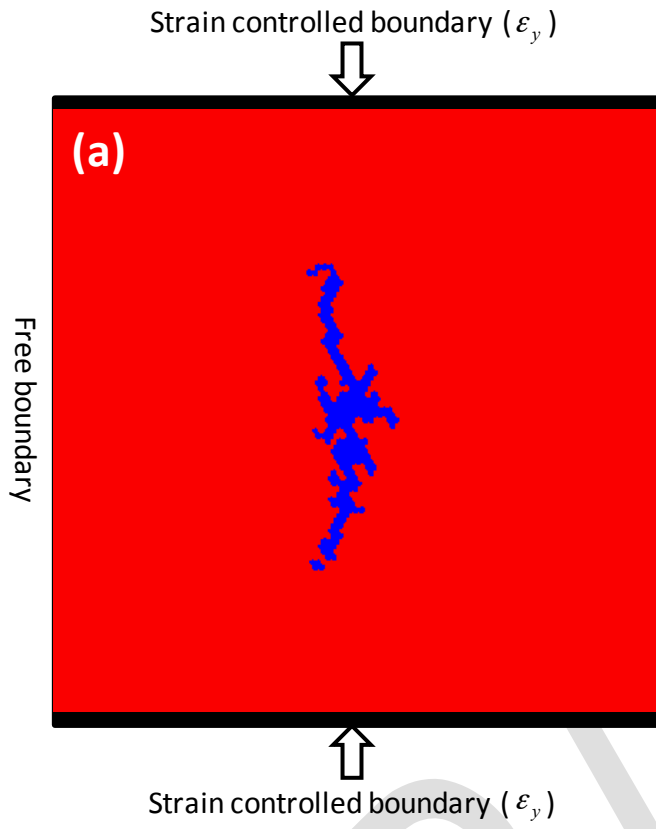
13

14

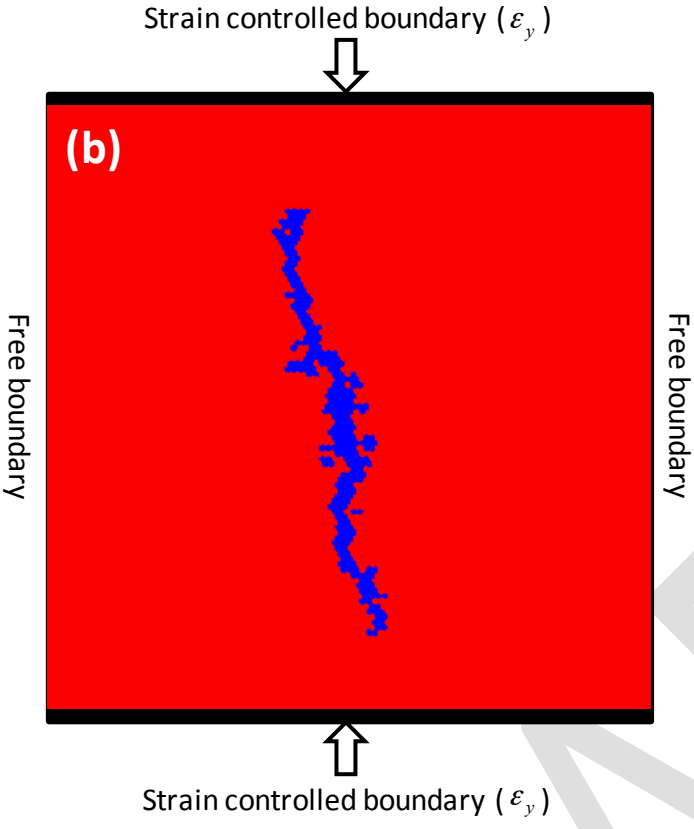


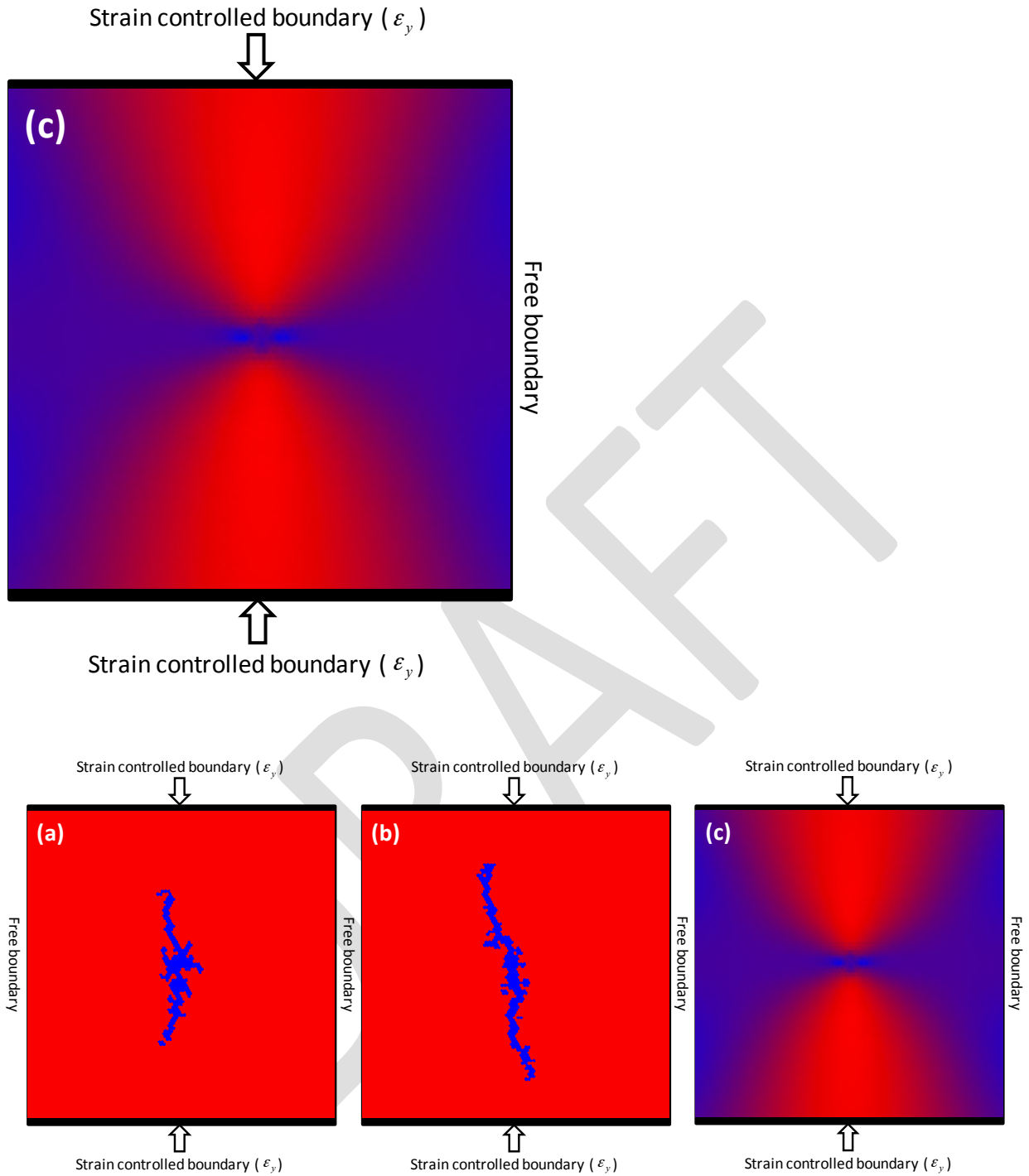
3 **Fig. (I).** Schematic diagram of ADI solution of Finite-difference pressure continuum, after
 4 [Wang and Chen, 2001].

1 **Appendix-B:**



2





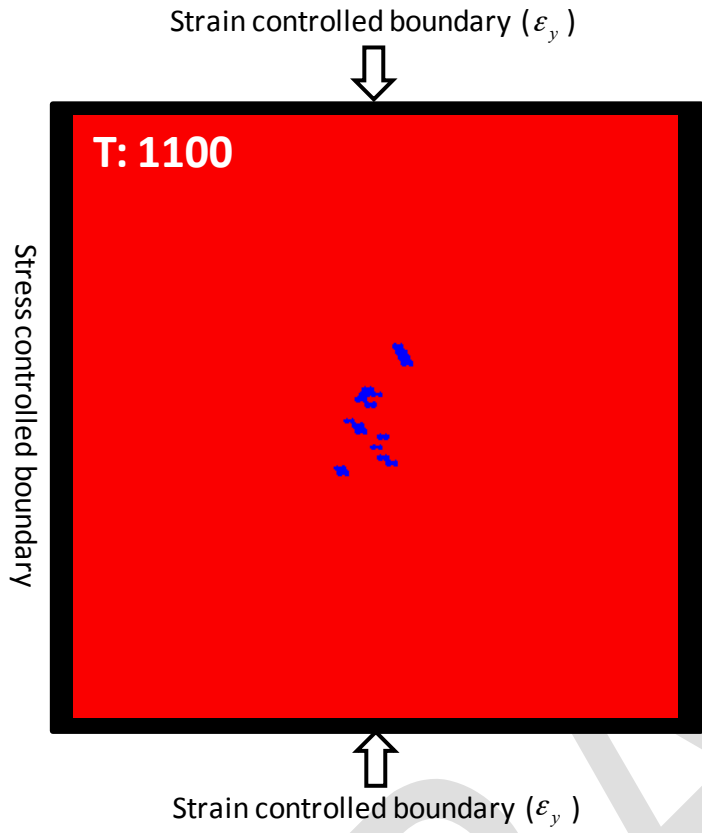
3 **Fig. (II).** Different patterns of hydro-fractures in a situation where a constant point source is
 4 injected in a homogeneous media under different remote stresses: (a) with relative smaller σ_y ,
 5 the results show the initial development of circular fracturing at the source location (centre) with

1 elongated fractures oriented parallel to the axis of the applied stress. In contrast to the pattern
2 shown in (a), in (b) a larger σ_y dominates the overall pattern and results only in sub-vertical
3 oriented fractures parallel to the main stress axis and through the source location (central). (c)
4 The figure shows the state of stress field at the onset of fracturing, where the red color code
5 represents high differential stress and blue low differential stress.

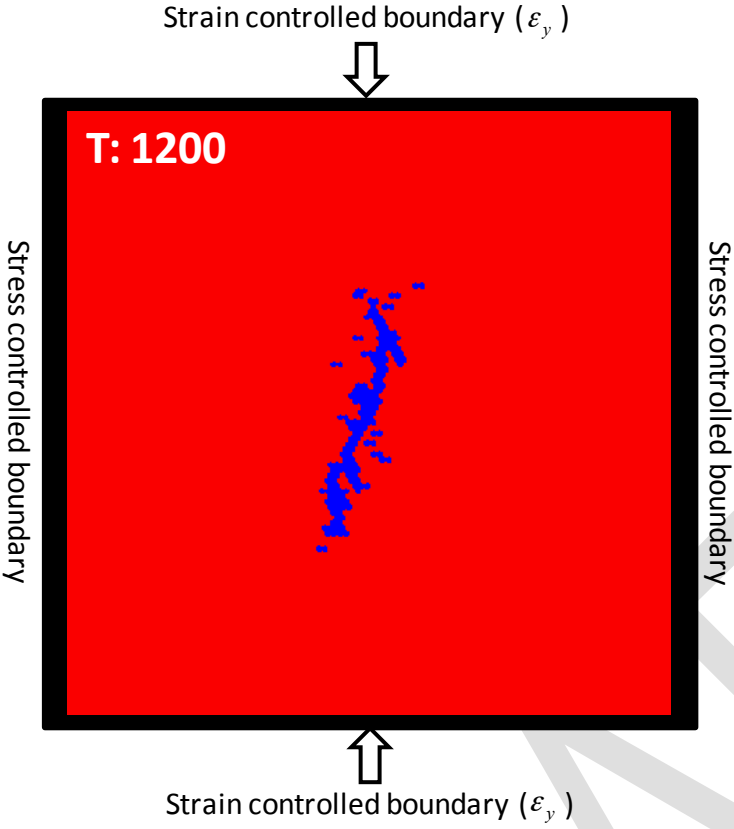
6
7
8
9
10
11
12
13
14
15
16
17
18
19
20
21
22
23



1 **Appendix-C:**



DRAFT



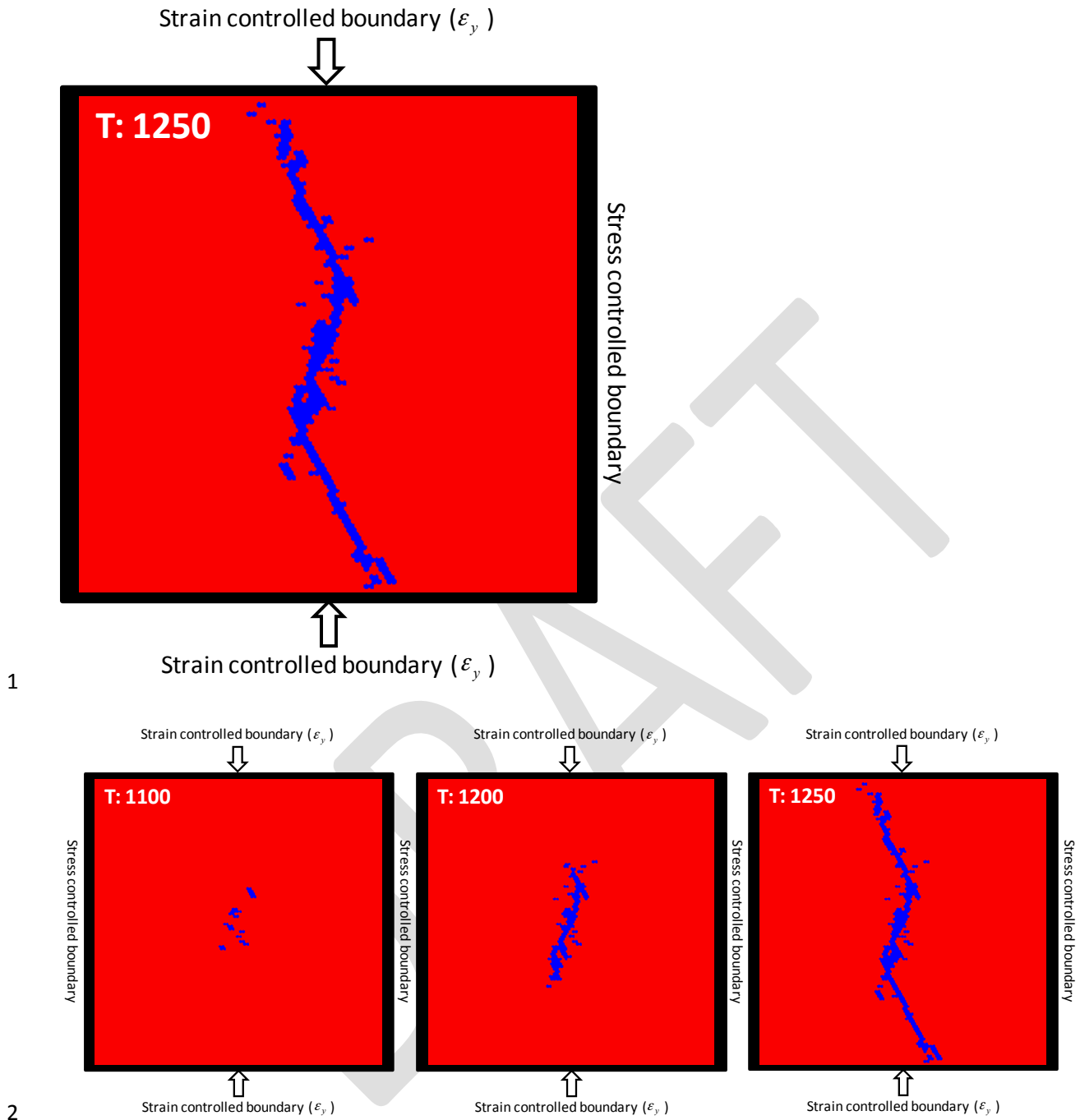


Fig. (III). This figure shows a time series illustrating the influence of the local pore overpressure on brittle failure in a pure shear stress regime. In this case the extension fractures develop at the source location (centre) and link up with shear fractures onwards the edges of the simulation box (time steps T increase from left to right).